Published in final edited form as:

Neuron. 2022 August 17; 110(16): 2588–2606.e6. doi:10.1016/j.neuron.2022.05.024.

Presynaptic FMRP and local protein synthesis support structural and functional plasticity of glutamatergic axon terminals

Hannah R. Monday[*,#,1,4], **Shivani C. Kharod**[#,1], **Young J. Yoon**[1,2], **Robert H. Singer**[2], **Pablo E. Castillo**[*,1,3,5]

[1] Dominick P. Purpura Department of Neuroscience, Albert Einstein College of Medicine, 1300 Morris Park Avenue, Bronx, NY, 10461, USA

[2] Department of Cell Biology, Albert Einstein College of Medicine, 1300 Morris Park Avenue, Bronx, NY, 10461, USA

[3] Department of Psychiatry and Behavioral Sciences, Albert Einstein College of Medicine, 1300 Morris Park Avenue, Bronx, NY, 10461, USA

[4] Current address: Department of Molecular and Cellular Biology, and Helen Wills Neuroscience Institute, University of California, Berkeley, Berkeley, CA 94720, USA.

[5] Lead contact

SUMMARY:

Learning and memory rely on long-lasting, synapse-specific modifications. While postsynaptic forms of plasticity typically require local protein synthesis, whether and how local protein synthesis contributes to presynaptic changes remains unclear. Here, we examined the mouse hippocampal mossy fiber (MF)-CA3 synapse which expresses both structural and functional presynaptic plasticity and contains presynaptic Fragile X messenger ribonucleoprotein (FMRP), an RNA-binding protein involved in postsynaptic protein synthesis-dependent plasticity. We report that MF boutons contain ribosomes and synthesize protein locally. Long-term potentiation of MF-CA3 synaptic transmission (MF-LTP) was associated with translation-dependent enlargement of MF boutons. Remarkably, increasing *in vitro* or *in vivo* MF activity enhanced protein synthesis in MFs. Moreover, deletion of presynaptic FMRP blocked structural and functional MF-LTP, suggesting that FMRP is a critical regulator of presynaptic MF plasticity. Thus, presynaptic

[*] To whom correspondence should be addressed: Pablo E. Castillo, MD/PhD, Dominick P. Purpura Department of Neuroscience, Albert Einstein College of Medicine, 1410 Pelham Parkway South, Kennedy Center, Room 703, Bronx, NY 10461, USA, pablo.castillo@einsteinmed.edu, Hannah R. Monday, PhD, Dominick P. Purpura Department of Neuroscience, Albert Einstein College of Medicine, 1410 Pelham Parkway South, Kennedy Center, Room 703, Bronx, NY 10461, USA, hannah.monday4@gmail.com.
[#]These authors contributed equally.

Author Contributions: Conceptualization, H.R.M., P.E.C, S.C.K., Y.J.Y., R.H.S.; Methodology, H.R.M., Y.J.Y.; Investigation, H.R.M. and S.C.K.; Resources, Y.J.Y., R.H.S., P.E.C.; Writing-Original Draft, H.R.M. and P.E.C.; Writing-Review and Editing, all authors; Visualization; H.R.M., S.C.K.; Supervision, H.R.M. and P.E.C., Funding Acquisition, H.R.M., Y.J.Y., R.H.S., P.E.C.; Project Administration, P.E.C.

The authors declare no competing interests.

FMRP and protein synthesis dynamically control presynaptic structure and function in the mature mammalian brain.

In Brief

Monday, Kharod et al. report that neuronal activity regulates presynaptic FMRP function and local synthesis of β-actin. In vitro activity and in vivo experience engage FMRP-dependent spatiotemporal regulation of protein synthesis that is required for presynaptic remodeling and long-term changes in neurotransmitter release.

Graphical Abstract

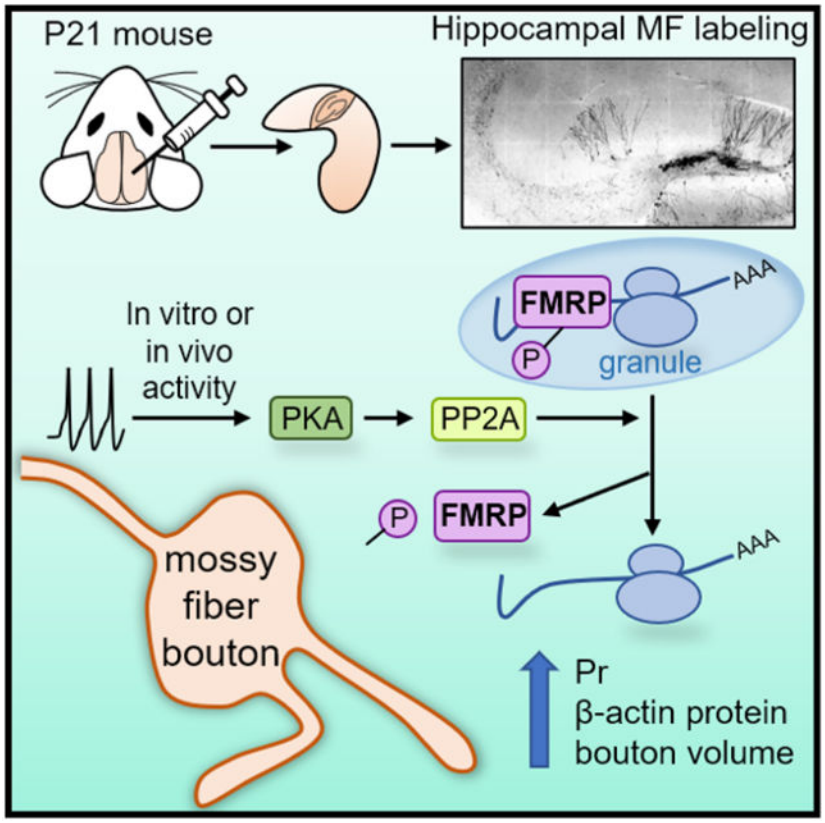

INTRODUCTION

Protein synthesis plays a critical role in long-term memory formation (Costa-Mattioli et al., 2009; Mayford et al., 2012) by supporting structural changes at synapses (Bailey et al., 2015; Sutton and Schuman, 2006). Synaptic plasticity can result from activity-dependent changes in either or both pre- and postsynaptic compartments. Many forms of postsynaptically-expressed plasticity require local protein synthesis (Holt et al., 2019). Previous research suggests that certain forms of long-term presynaptic plasticity may rely on local protein synthesis (Hafner et al., 2019; Yin et al., 2006; Younts et al., 2016), but the molecular functions of locally synthesized proteins in presynaptic compartments remain unclear. Dysregulation of synaptic protein synthesis may be a convergent feature of Autism

Spectrum Disorders (ASDs) (Bourgeron, 2015; Klein et al., 2016; Louros and Osterweil, 2016), including Fragile X Syndrome (FXS) (Bagni and Zukin, 2019; Darnell and Klann, 2013). However, the regulatory mechanisms of local presynaptic translation are poorly understood.

To explore the role of local translation in presynaptic plasticity, we took advantage of the mossy fiber (MF) axons in the hippocampus as a model system. The MF axons extend from granule cells (GC) in the dentate gyrus (DG) and project through the stratum lucidum to the CA3 region, where they synapse on CA3 pyramidal cells and interneurons (Acsady et al., 1998; Evstratova and Toth, 2014; Henze et al., 2000). MFs form a distinct bundle of unmyelinated fibers that make giant synapses onto the thorny excrescences protruding from proximal dendrites of CA3 pyramidal cells (MF-CA3) (Acsady et al., 1998; Claiborne et al., 1990) and smaller, filopodial and *en passant* synapses onto local interneurons (Acsady et al., 1998; Lawrence et al., 2004). MF-CA3 synapses undergo presynaptically-expressed, NMDA receptor-independent long-term potentiation (MF-LTP) and long-term depression (MF-LTD) (Nicoll and Schmitz, 2005). As the primary excitatory drive to the hippocampus proper, MFs are critical for hippocampus-dependent forms of learning and memory (Acsady and Kali, 2007; Rolls, 2013). Mechanistically similar forms of LTP/LTD have been identified in other brain areas (Castillo, 2012; Monday et al., 2018). MFs undergo dynamic remodeling under conditions of strong activity (Chierzi et al., 2012; De Paola et al., 2003; Maruo et al., 2016; Zhao et al., 2012), including epilepsy (Danzer et al., 2010; Sutula and Dudek, 2007), enriched environment (Galimberti et al., 2006; Gogolla et al., 2009), and spatial learning (Routtenberg, 2010).

The mechanisms by which activity leads to a presynaptic structural change are poorly understood, although a requirement for protein synthesis has been suggested (De Paola et al., 2003). Importantly, translation is also required for MF-LTP, but whether protein is made locally or trafficked from the soma is unclear (Barnes et al., 2010; Calixto et al., 2003). Though local presynaptic protein synthesis has been suggested at the MF-CA3 synapse (Huang and Hsu, 2004; Huang et al., 1994), there is conflict in the literature (Barnes et al., 2010; Calixto et al., 2003) and it has never been directly demonstrated. Moreover, the relationship between presynaptic activity, structural change and local protein synthesis is not clear, nor is the identity of presynaptically synthesized proteins.

The precise amount and identity of locally synthesized protein is critical for synaptic plasticity. RNA-binding proteins are key regulators of activity-dependent local protein synthesis in neuronal processes (Klein et al., 2016). Fragile X messenger ribonucleoprotein (FMRP) is an RNA-binding protein with well-characterized roles in mRNA localization and translation repression (Bagni and Zukin, 2019; Darnell and Klann, 2013). FMRP has been identified in a subset of presynaptic terminals throughout the brain including the MF synapse (Akins et al., 2017; Christie et al., 2009). A loss-of-function mutation in the *FMR1* gene that encodes FMRP leads to FXS, the most common monogenic cause of syndromic ASD (Hagerman et al., 2011). Under basal conditions, FMRP interacts with polyribosomes and mRNAs to form a granule (Brown et al., 2001; Lai et al., 2020), which is trafficked along neuronal processes in a translationally-repressed state (Antar and Bassell, 2003; Darnell et al., 2011; Dictenberg et al., 2008). Activity-dependent dephosphorylation

of FMRP by protein phosphatase 2A (PP2A) triggers granule disassembly and de-repression of translation (Narayanan et al., 2007). FMRP-mediated regulation of the localization and translation of dendritic mRNA controls postsynaptic forms of plasticity (Bagni and Zukin, 2019). The function of FMRP at the presynapse has not been well-defined, but may be related to translational repression (Akins et al., 2017; Chyung et al., 2018). *Fmr1* KO mice have impaired actin dynamics and dysregulation of pre- and postsynaptic structures (Michaelsen-Preusse et al., 2018; Scharkowski et al., 2018), presumably through the upregulation of local protein synthesis. However, to our knowledge, the specific role of presynaptic FMRP in activity-dependent structural plasticity in the mammalian brain has never been tested.

Here, we demonstrate the capacity of mossy fiber boutons (MFBs) to synthesize protein locally in acute hippocampal slices. We discover that MFBs contain protein synthesis machinery and MF-LTP is associated with increases in local presynaptic β-actin synthesis in MFBs. In addition, MF-LTP involves rapid, translation-dependent remodeling of MFBs and disassembly of FMRP granules, associated with PP2A and PKA-dependent translational de-repression. Using a conditional KO strategy, we show that loss of presynaptic FMRP impairs structural and functional MF-LTP, and increases local protein synthesis in the MF tract. Lastly, exposing animals to enriched environment (EE) led to increased overall protein synthesis in the MF tract, and even greater protein synthesis increase was induced by loss of presynaptic FMRP. Together, our findings provide strong evidence for the regulation of protein synthesis by presynaptic FMRP in presynaptic structural and functional plasticity at excitatory presynapses in the mature brain.

RESULTS

MFs synthesize actin locally

Given that mature MFBs are structurally dynamic (Galimberti et al., 2006), we tested whether β-actin can be synthesized locally in MFBs by optimizing a Halo-actin protein synthesis reporter system for use in the mouse brain (Yoon et al., 2016). β-actin mRNA is highly abundant in the neuropil (Buxbaum et al., 2014; Cajigas et al., 2012) where its activity-induced translation could underlie structural plasticity of dendritic spines (Yoon et al., 2016) and growth cone remodeling (Leung et al., 2006). Our reporter system expresses β-actin protein fused to the Halotag, along with the endogenous 3’ UTR of the β-actin mRNA to allow normal mRNA localization. The bath application of ultra-bright, membrane-permeable JF dyes conjugated to the Halotag ligand (JF-HTL) allow for labeling of the Halotag fusion proteins with very high affinity and specificity (Grimm et al., 2015). We stereotactically injected a high-titer lentivirus of the Halo-actin construct specifically into the DG, which resulted in sparse labeling of GCs (Figure 1A). Newly synthesized actin was detected using a pulse-chase experiment as follows: bath application of the first dye (i.e. JF549-HTL) binds the entire population of pre-existing Halo-actin with an essentially irreversible covalent bond. Next, excess dye was washed out for 30 minutes, then the second dye (i.e. JF646-HTL) was bath applied, to label only the Halo-actin that has been newly synthesized in the intervening time window (~1.5 hours). We found that this approach detected newly synthesized actin in MFBs (Figure 1B). To test that our approach

was optimal for specifically measuring newly synthesized protein, we applied the protein synthesis inhibitor cycloheximide (CHX) during the 1st wash and second dye application. CHX reduced JF646 labeling to background levels in MFBs (Figure 1B), indicating that JF646 was selectively binding and reporting newly synthesized actin.

To test whether Halo-actin protein could be synthesized locally, we transected slices, making a small cut to sever the GC somas from the MF axon to prevent any trafficking of proteins from the GC soma to the MFBs (see Supp. Figure 1A for representative image), followed by sequential labeling of Halo-actin. We found that MFBs were still able to synthesize Halo-actin at the same level as nontransected slices (Figure 1C), and there was no difference in the ratio of pre-existing to newly synthesized actin in transected slices (Supp. Figure 1B), suggesting that under our experimental conditions local protein synthesis is the primary contributor to the newly synthesized actin in MFBs. Importantly, reversing the order of the dye had no effect on the detection of newly synthesized proteins (Supp. Figure 1C). Together, these data strongly suggest that Halo-actin protein can be synthesized locally in MFBs.

To assess local protein synthesis with high temporal resolution in nontransected MF axons, we took advantage of a photoactivatable (PA) Halo dye (Grimm et al., 2016). We bath-applied JF549-HTL and PA-JF646-HTL to acute hippocampal slices using the same pulse-chase paradigm described above. After washing out excess PA-JF646, we photoactivated (1 s, 25 mW, 40X obj., 0.8 NA) specifically in the CA3b region where our recordings and structural analysis are performed (see below), to capture only newly made Halo-actin in MFBs (Figure 2A). We found that photoactivation revealed significantly more Halo-actin in MFBs than in control slices that still received the PA-JF646 dye, but no photoactivation (Figure 2B). These data are consistent with newly synthesized Halo-actin at MFBs. However, we cannot exclude fast axonal trafficking of new Halo-actin from the GC soma, a possibility that seems unlikely in a 1-hour time window given the estimated axonal transport rates of actin (2–8 mm/day) (Roy, 2020) –e.g. a protein synthesized in the GC soma would take 3–12 hours to reach MFBs in CA3b approximately 1 mm away. To assess the temporal dynamics of Halo-actin trafficking in MFBs, we performed additional experiments wherein we photoactivated Halo-actin in GC somas and measured the fluorescence intensity of PA-JF646 at two time windows (1 hour and 3.5 hours) following photoactivation, where the wash time was the same between both groups. We identified MFBs based on their morphological characteristics and expression of Halotag in stratum lucidum, indicated by antibody labeling. 1 hour post-PA, PA-JF646 labeled Halo-actin was not present in CA3b MFBs above the levels in control slices with no somatic photoactivation (Figure 2C), whereas we began to detect Halo-actin in this area after 3.5 hours (Figure 2D). Summary data showed significant difference in all three CA3 subregions between the two timepoints (Figure 2E,F). These results indicate that Halo-actin can be made locally in MFBs in intact slices in 1 hour, whereas somatic Halo-actin requires a longer time to be trafficked into MFBs of the CA3b region.

MFBs contain ribosomes

Given our data showing local synthesis of actin, we next examined if the protein synthesis machinery was present in MFBs. Resolving ribosomes in presynaptic terminals is challenging with conventional antibody labeling, therefore we utilized a cell-specific genetic strategy to detect ribosomes in axons (Shigeoka et al., 2016). The Ribotag mouse has loxP sites flanking the exon 4 of the large subunit ribosomal protein 22 (RPL22) genomic loci enabling Cre recombinase induced expression of endogenous RPL22 with a hemagglutinin-tag ($RPL22^{HA}$)(Sanz et al., 2009). $RPL22^{HA}$ has been previously reported to almost exclusively fractionate with polysomes, indicating that it is localized to assembled ribosomes, and ribosome run-off assays indicate ~80% of $RPL22^{HA}$-labeled ribosomes are actively translating (Sanz et al., 2009; Shigeoka et al., 2016). To achieve GC-specific expression of $RPL22^{HA}$ and sparse fluorescent labeling of MFBs, we injected lentivirus encoding ChiEFtom2A-Cre or ChiEFtom2A-GFP for Controls under the control of the C1QL2 promoter (Barthet et al., 2018) into the dentate gyrus of the Ribotag mice, resulting in expression of channelrhodopsin (ChiEF) fused to tdTomato and Cre or GFP. The ChiEFtom2A fusion protein provides a membrane delimited MFB label within which we quantified the HA signal in both groups. In control GFP-expressing (Cre-negative) mice, no HA immunolabeling was detectable in the GC soma, axons, or MFBs as expected (Figure 3A). In the Cre-positive slices, $RPL22^{HA}$ labeling was evident in the cytoplasm and nucleoli of GCs somas, but largely excluded from the nucleus as anticipated, and significantly increased in the MFBs above background levels of HA staining in GFP controls (Figure 3B,C), strongly suggesting that MFBs contain ribosomes. We defined ribosome-containing boutons as those with 10-fold the HA intensity relative to the mean value of HA (i.e. 0.02 A.U.) in GFP Control boutons. 65% of the MFBs we measured met this criteria whereas 0% of MFBs from Controls did (Figure 3D). MFBs containing ribosomes were evenly distributed throughout the CA3 axis with the highest HA intensity localized to CA3b (Figure 3E).

MF-LTP involves protein synthesis-dependent structural and functional changes

Given that postsynaptic plasticity is associated with activity-dependent local protein synthesis (Nakahata and Yasuda, 2018), including β-actin (Yoon et al., 2016), we sought to determine whether presynaptic MF-LTP is also associated with local protein synthesis by measuring new Halo-actin synthesis specifically in MFBs as in Figure 1. We found that delivering a MF-LTP induction protocol (see Methods) resulted in an increase (28% ± 13%) in Halo-actin levels 1 hour later compared to sham slices which were placed in the recording chamber but did not undergo LTP induction (Figure 4A,B), indicating that MF-LTP is associated with actin synthesis in MFBs. The frequency of boutons with the lowest Halo-actin intensity was reduced in slices that received the LTP induction protocol, suggesting activity may convert MFBs from a translationally quiescent to active state (Figure 4C).

In order to determine whether MF-LTP-induced changes in Halo-actin levels might be linked to regulation of MFB structure, we investigated whether potential structural changes associated with MF-LTP required protein synthesis. To achieve sparse labeling and optogenetic control over MFBs, we injected the C1QL2-ChiEFtom2A-Cre or -GFP lentivirus as in Figure 3 (Figure 5A). Using ChiEFtom2A as a fluorescent label, we

reconstructed the MFBs in 3D with Imaris software to perform unbiased MFB detection and volumetric measurement. Optogenetic activation of GC axons (i.e. MFs) in acute slices (Figure 5B) led to increased MFB volume measured 1 hour after LTP induction. Blockade of translation by bath application of 80 μM CHX (pre-incubated for 15 minutes and present throughout experiment) prevented the MF-LTP-induced increase in bouton volume, but CHX alone had no significant effect on basal bouton volume (Figure 5C,D,E). CHX also had no effect on basal MF transmission (Supp. Figure 2A). MF-LTP and CHX had no significant effect on filopodial length or number (Figure 5F,G).

To test whether functional MF-LTP (i.e. LTP of MF-CA3 synaptic transmission) requires local protein synthesis, we performed recordings in acute WT mouse hippocampal slices where we made a small cut to sever the GC somas from the presynapse (Figure 5H), as in Figure 1. Transecting MFs had no effect on the induction or expression of MF-LTP, but MF-LTP was impaired by bath application of the protein synthesis inhibitor CHX (Figure 5H). Taken together, these results demonstrate that MF-LTP is correlated with enhanced local β-actin synthesis and protein synthesis is required for both synaptic strengthening and enlargement of bouton volume.

Loss of FMRP impairs MF activity-dependent protein synthesis as well as structural and functional MF-LTP

MFBs express the mRNA translational repressor FMRP (Christie et al., 2009) which has been implicated in local postsynaptic protein synthesis-dependent plasticity (Bagni and Zukin, 2019; Christie et al., 2009). We hypothesized that FMRP regulates MF plasticity by modulating local protein synthesis. To quantify the rate of protein synthesis in MFs, we used a brief pulse of puromycin in acute hippocampal slices to tag nascent peptides (Hafner et al., 2019; Schmidt et al., 2009). Given the unique concavities and tight association of the MFB and postsynaptic structure resolving the pre- and postsynaptic compartment at the MF synapses is difficult even using super-resolution microscopy. To rule out an increase in postsynaptic activity from electrical MF-LTP induction as a potential confounding factor in meaurements of puromycin in the MF tract (stratum lucidum) we induced MF-LTP in WT mice in the presence of antagonists of ionotropic and metabotropic glutamate receptors (5 μM NBQX, 50 μM d-APV, 4 μM MPEP, 50 μM LY367385) to block excitatory synaptic transmission. MF-LTP was associated with significantly increased puromycin labeling in the MF tract (i.e. stratum lucidum) in the presence of synaptic antagonists but not stratum radiatum (Supp. Figure 3A), suggesting that the increase in protein synthesis is presynaptic in origin and not a result of increased postsynaptic activity. As previously reported (David et al., 2012), we confirmed that protein synthesis was blocked by anisomycin, a competitive inhibitor of puromycin that blocks translation elongation by binding to the peptidyl-transferase center (Grollman, 1967), but not CHX, an elongation inhibitor that binds downstream of puromycin in the E site of the ribosome (Supp. Figure 3B). Control experiments demonstrated the specificity of the puromycin antibody (Supp. Figure 3C).

In slices from *Fmr1*$^{fl/fl}$ mice in which FMRP was conditionally deleted from presynaptic GCs via targeted injection of AAV-CAMKII-mCherry-Cre (cKO), protein synthesis was increased under basal conditions in stratum lucidum (where the MFBs reside), consistent

with the reported function of FMRP as a negative regulator of synaptic translation (Antar and Bassell, 2003; Darnell et al., 2011; Lai et al., 2020), and was further increased by LTP induction compared to control slices injected with AAV-CAMKII-mCherry (Figure 6A,B). In contrast, protein synthesis measurements from stratum radiatum, where FMRP expression was intact, were not altered by LTP inducton or cKO of *Fmr1* (Supp. Figure 3D). For these experiments, AAV was used to achieve higher population of Cre expressing cells and thus FMRP loss in MFBs (Supp. Figure 4). While these results suggest that FMRP is not responsible for bulk control of activity-dependent protein synthesis in the MFB, FMRP could still be involved in selective activity-dependent control of a subset of mRNAs.

Fmr1 KO mice exhibit deficits in MFB density (Ivanco and Greenough, 2002; Mineur et al., 2002) and altered presynaptic plasticity at other CNS synapses (Deng et al., 2011; Koga et al., 2015), suggesting that FMRP may be important for regulating activity-dependent structural and functional MF plasticity. FMRP has not been reported to bind β-actin mRNA directly (Ascano et al., 2012; Eliscovich et al., 2017), (but see (Darnell et al., 2011). However, FMRP could participate in MFB structural plasticity via indirect regulation of the translatability of β-actin mRNA (Buxbaum et al., 2014) or the direct translational regulation of other cytoskeletal proteins (Feuge et al., 2019). To determine if presynaptic FMRP is involved in the regulation of activity-dependent presynaptic structural modifications, we characterized the structural changes associated with MF-LTP in acute hippocampal slices from *Fmr1* cKO mice (Mientjes et al., 2006). We injected *Fmr1* floxed mice with LV-C1QL2-ChiEFtom2A-Cre or LV-C1QL2-ChiEFtom2A-GFP for controls. Although MF-LTP was associated with an increase in MF bouton volume in control mice, this increase was not seen in *Fmr1* cKO mice (Figure 6C–E). Loss of presynaptic FMRP increased filopodial length irrespective of LTP (Figure 6F), but did not effect filopodial number in cKO mice (Figure 6G). Furthermore, using extracellular field recordings of MF-CA3 transmission, we found that loss of presynaptic FMRP significantly impaired MF-LTP in cKO slices compared to WT controls (Figure 6H). Therefore, presynaptic FMRP is a critical modulator of activity-dependent structural plasticity and functional MF plasticity.

PKA and PP2A regulate activity-dependent FMRP granule assembly, protein synthesis, FMRP phosphorylation, and MF-LTP.

mRNAs are transported in granules that carry mRNA-binding proteins such as FMRP and ribosomes in a translationally-repressed state (Antar et al., 2005; Lai et al., 2020) (Chyung et al., 2018). To determine whether MF activity caused changes in FMRP granule structure, such as disassembly events that could be used as indications of translational activation, we injected a lentivirus encoding mouse FMRP fused to Halotag (Halo-FMRP) in GCs. Expression of this construct in hippocampal neuron culture revealed strong colocalization of the Halo-FMRP with endogenous FMRP in neuronal somas and neurites (Supp. Figure 5A). Upon expressing Halo-FMRP in GCs and labeling it in slices through bath application of JF549-HTL (200 nM) (Grimm et al., 2015), we detected FMRP localized to MFBs, in agreement with previous reports (Figure 7A) (Akins et al., 2017; Christie et al., 2009). Assembled axonal FMRP granules were identified by high intensity fluorescent Halo-FMRP puncta with sizes in the range of 0.2–1 μm^2 in MFBs, whereas sites of granule disassembly were indicated by patches of diffuse lower intensity puncta with an area between 3 – 30

μm^2 (Figure 7B). We controlled for potential differences in viral expression between slices by splitting slices from the same animal into each condition and measuring the ratio of the number of ‘ disassembled’ to ‘ assembled’ granules per slice. We found that the electrical MF-LTP induction protocol led to increased ratio of ‘ disassembled’ granules in acute hippocampal slices, suggesting translational activation (Lai et al., 2020; Narayanan et al., 2007) (Figure 7D,C). Similarly, the ratio was also increased by transient bath application of the adenylyl cyclase activator forskolin (FSK, 50 μM for 10 min), a manipulation that induces chemical LTP of MF-CA3 transmission via PKA activation (Nicoll and Schmitz, 2005). Moreover, the size of ‘ assembled’ FMRP granules was also reduced in both forms of LTP induction (Figure 7D,E), further suggesting that activity biases granules towards dissassembly. Previously, activity-dependent dephosphorylation of FMRP by PP2A has been implicated in FMRP granule disassembly and translational de-repression (Narayanan et al., 2007; Tsang et al., 2019). Consistent with this observation, the addition of PP2A inhibitor, okadaic acid (OKA, 25 nM), abolished the reduction in granule size following MF-LTP and FSK application (Supp. Figure 5B). Together, these data not only support a presynaptic localization of FMRP, but also indicate that FMRP granules disassemble during MF-LTP.

Next, we hypothesized that mechanisms regulating granule assembly should also regulate protein synthesis if the two processes are linked. We measured protein synthesis in the MF tract using puromycin labeling as in Figure 6A. We found that PKA activation with forskolin and electrical MF-LTP both were associated with increased protein synthesis. This increase in protein synthesis was blocked by application of the PP2A inhibitor okadaic acid or PKA inhibitor, PKI (Figure 7F,G). Okadaic acid application reduced basal protein synthesis, whereas PKI did not (Supp. Figure 5C). PP2A-mediated control of FMRP granule assembly occurs through the phosphorylation and dephosphorylation at the serine 499 (Ser499) residue of FMRP. To test if this phosphorylation site was affected by PKA activation, we performed immunohistochemistry for pFMRP-(Ser499) in the GC layer in hippocampal slices. Consistent with our Halo-FMRP findings, phosphorylation of FMRP was also regulated by PKA activation in a PP2A dependent manner. PKA activation reduced levels of phosphorylated FMRP suggesting granule disassembly, and this reduction was blocked by pre-incubation with PP2A inhibitor okadaic acid (Figure 7H). Thus, if MF-LTP relies on granule assembly and protein synthesis, it should be blocked by PP2A inhibition. We tested this possibility using extracellular field recordings of MF-CA3 transmission. MF-LTP was blocked by bath application of okadaic acid, suggesting that PP2A activity is required for MF-LTP (Figure 7I).

Enriched environment alters the functional and structural properties of MFs

Enriched environment (EE), an *in vivo* manipulation known to increase the activity of GCs, enhances filopodial motility and bouton complexity (Caroni et al., 2012; Galimberti et al., 2006; Gogolla et al., 2009). Given our findings that MF-LTP is associated with increased bouton volume and protein synthesis, we decided to test whether in vivo experience impact MF-LTP, structure and protein synthesis in MFBs in an FMRP-dependent manner. We exposed mice to EE in a large cage with toys and running wheels (Supp. Figure 6A) starting at P21 until P36–46 (Figure 8A) and compared them to the mice housed in Home cages (HC). EE impaired MF-LTP and was associated with a reduction in PPR at baseline,

suggesting that EE occluded the expression of LTP (Supp. Figure 6B,C). EE led to a subtle increase in MF bouton volume compared to HC controls (Figure 8B–D). MFBs from EE mice had significantly longer filopodia with no significant change in the number of filopodia/bouton (Figure 8E,F). It should be noted that our bouton volume measurements include the main bouton and all filopodia, thus it is possible that the increase in filopodia length is a primary contributor to the measured increase in bouton volume. Thus, EE induces specific structural changes in MFBs that are similar but distinct from those induced by MF-LTP. We also measured gross anatomical features of the MF tract, and found that the infrapyramidal bundle of MFs was significantly longer in the EE exposed animals, as reported previously (Romer et al., 2011), but there was no change in the width or length of stratum lucidum (i.e. the suprapyramidal bundle) (Supp. Figure 6D).

To determine if these experience-induced changes at the MF were associated with changes in protein synthesis, we measured Halo-actin synthesis in individual MFBs (Figure 8G). Surprisingly, we found that EE led to a reduction in newly synthesized Halo-actin in boutons but an increase in newly synthesized actin in filopodia of MFBs (Figure 8G), consistent with the increase in filopodial length (Figure 8E). Finally, to assess whether EE resulted in changes in overall newly synthesized protein levels in the MF tract, we performed puromycin labeling as in Figure 6. We discovered that EE led to significant increases in puromycylated nascent peptides in the MF tract (Figure 8H). We also tested whether EE altered newly synthesized protein levels in mice with presynaptic cKO of *Fmr1* from GCs. We found that *Fmr1* cKO slices displayed significantly enhanced protein synthesis regardless of housing condition. Together these data indicate that *in vivo* activity of MFs leads to specific changes in presynaptic structure and protein synthesis.

DISCUSSION

Here, we provide evidence that protein synthesis supports presynaptic structural remodeling associated with presynaptic plasticity. We demonstrate that MFBs can synthesize proteins locally and and contain RPL22, an essential component of translating ribosomes. Moreover, our data demonstrate that protein synthesis in the MF tract is regulated by *in vitro* and *in vivo* activity, which has distinct effects on the structure of MFBs and the local synthesis of a candidate protein, actin. These findings are significant in that protein synthesis is a key mechanism of dendritic spine remodeling associated with postsynaptic forms of plasticity (Nakahata and Yasuda, 2018; Sutton and Schuman, 2006), but its presynaptic function has been heretofore unclear. Along with local protein degradation, local regulation of energy production, and local structural change (Cohen and Ziv, 2017; Monday et al., 2020), the general acceptance that local protein synthesis occurs in presynaptic compartments supports the notion that presynaptic compartments are discrete, computationally-independent units, akin to dendritic spines.

Local protein synthesis in excitatory presynaptic boutons

Despite the long-standing dogma that mature mammalian axons and presynaptic terminals do not synthesize proteins, recent evidence to the contrary has amassed, including isolation and identification of presynaptic mRNAs (Akins et al., 2017; Hafner et al., 2019; Ostroff

et al., 2019; Shigeoka et al., 2016), visualization of presynaptic ribosomes, translation elongation/initiation factors, and RNA-binding proteins (Akins et al., 2017; Hafner et al., 2019; Ostroff et al., 2019; Scarnati et al., 2018; Shigeoka et al., 2016; Younts et al., 2016), evidence for altered neurotransmitter release with protein synthesis inhibition (Scarnati et al., 2018; Younts et al., 2016), and roles for presynaptic protein synthesis in behavior (Ostroff et al., 2019) in a wide variety of model systems. Selectively targeting or measuring local protein synthesis in subneuronal compartments is a difficult technical challenge because of the small scale of these structures (Holt et al., 2019; Iwasaki and Ingolia, 2017). We took advantage of the large presynaptic MFBs and used multiple approaches to measure local protein synthesis. First, we optimized the Halo-actin reporter system for broad use in intact brain circuits (Yoon et al., 2016). By injecting the Halo-actin reporter virus directly into the DG, we were able to selectively express it in GCs, affording us the spatial resolution to isolate and visualize presynaptic protein synthesis. Using physical transection of MF axons and local photoactivation of JF dyes, we found that local synthesis is a significant contributor to the pool of newly synthesized presynaptic actin. In our slices, the average length of MF axons from the GCs to CA3b subregion was ~ 1 mm. Given published rates of axonal transport of actin are ~2–8 mm/day (Roy, 2020), a β-actin protein moving at the maximal velocity would still require ~ 3 hours to reach CA3b from the hilus or GC soma. In agreement with these observations, our data (Figure 2) suggest that actin trafficking from GC somas/proximal axons to MFBs occurs to some extent after 3.5 hours, but not within 1 hour. Moreover, using cell-specific expression of a tagged ribosomal protein, we validated that a key component of the translation machinery is also present in MFBs.

Even considering multiple mRNAs and polyribosomes, the amount of newly synthesized β-actin likely represents only a small fraction of the large pool of actin at presynapses (Wilhelm et al., 2014), a number that likely varies substantially based on the synapse and preparation. Why then should actin be translated locally? One explanation is that spatiotemporally regulated posttranslational modifications may confer functional distinctions on newly synthesized proteins. It was proposed that newly synthesized β-actin may be more efficient at nucleation and polymerization of actin filaments (Shestakova et al., 2001), perhaps through fast arginylation at the N-terminus which has been previously shown to increase actin polymerization (Saha et al., 2010), or via chaperone binding to nascent β-actin chains to protect them from glutathionylation, which restricts the rate of polyermization (Shestakova et al., 2001). In addition, the relatively small size of the presynaptic compartment has been suggested to allow the local enrichment of newly synthesized actin monomers, further increasing its ability to create new nucleation sites (Leung et al., 2006). Thus, although the contribution of local translation to total subcellular protein content for highly abundant proteins may be small, the functional distinction of somatic versus locally synthesized proteins could be the primary effector of synaptic alterations. Moreover, the highly dynamic structure of MFBs could also explain high levels of local protein synthesis.

Additionally, we used puromycylation of nascent peptides (Schmidt et al., 2009) to study the rate of protein synthesis the MF tract (Figure 6). We found that *in vitro* LTP induction correlated with enhanced overall protein production levels and new actin synthesis in MFs. Furthemore, targeted deletion of FMRP increases protein synthesis in the MF tract under

basal conditions and more so during high activity (i.e. LTP and EE). We show that EE alone also leads to an enhancement of newly synthesized protein in the MF tract but a reduction in Halo-actin synthesis at the level of the single bouton. To better distinguish activity-induced changes in local protein synthesis in the presynaptic compartment, as opposed to postsynaptic compartments or perisynaptic astrocytic processes (Mazare et al., 2020), excitatory synaptic antagonists were used in order to prevent glutamate-mediated postsynaptic or astrocytic activation. Although, we cannot exclude that our protein synthesis measurements with puromycin include a contribution from the postsynaptic CA3 dendrite, the changes resulting from presynaptic FMRP deletion and presynaptic activation in the presence of excitatory synaptic antagonists suggest our experiments can detect changes in presynaptic axons and MFBs. Moreover, we used multiple additional mechanisms that support the general conclusion of activity-dependent protein synthesis in MFBs. MF-LTP is induced by a brief activation of GCs specifically (~ 1 minute), whereas EE enhances activity in a wide variety of hippocampal neurons over an extended period of time (2 weeks)(van Praag et al., 2000). EE also increases levels of neurotrophic factors like BDNF and the number of adult-born neurons in the DG (Kempermann et al., 1997). Therefore, homeostatic processes, like changes in inhibitory circuits, formation of new synapses, and/or changes in cellular excitability may potentially occur as a result of EE that could partially overlap with MF-LTP mechanistically.

Structural plasticity of MFBs

Presynaptic structural plasticity has been reported throughout the brain and can depend on the synapse type, the age of the animal, the size of the bouton, proximity of mitochondria and other organelles (Gogolla et al., 2007; Monday and Castillo, 2017; Smith et al., 2016). At MFs, structural plasticity is maintained by activity and synaptic remodeling may rely on differential activity among neighboring synapses where larger boutons undergo less structural remodeling (Chierzi et al., 2012; Maruo et al., 2016). While other studies looked at MF structural changes resulting from diverse forms of robust activity (De Paola et al., 2003; Maruo et al., 2016; Zhao et al., 2012), here we used repetitive burst stimulation of MF axons at 25 Hz (Ben-Simon et al., 2015; Castillo et al., 2002; Kaeser-Woo et al., 2013), to approximate sparse in vivo GC burst firing (10–50 Hz) (Diamantaki et al., 2016; Henze et al., 2002). To our knowledge, our study is also the first to demonstrate that this LTP-induced enhancement in MF bouton volume is dependent on protein synthesis.

At the molecular level, structural changes in MFBs may be critical for functional changes in synapse strength by regulating any number of nodes in the neurotransmitter release process. For example, structural plasticity could enable the insertion and unsilencing of new release sites, alter the coupling distance between calcium channels and primed vesicles, change the size of the active zone and the number of docked vesicles at a synapse, and alter clustering of the release machinery (Monday et al., 2018). Actin in the presynaptic terminal is involved in scaffolding of proteins, regulates neurotransmitter release and can be dynamically concentrated to the terminal during bouts of high activity (Morales et al., 2000; Sankaranarayanan et al., 2003). Actin dynamics therefore likely account for the structural remodeling and changes in neurotransmitter release we observed upon MF-LTP induction (Cingolani and Goda, 2008).

The role of presynaptic FMRP in MFB plasticity

Our study demonstrates that presynaptic FMRP plays a critical role in structural and functional MF plasticity. FMRP loss impairs actin dynamics (Feuge et al., 2019; Scharkowski et al., 2018). Although β-actin mRNA itself is not a bonafide FMRP target (Ascano et al., 2012; Eliscovich et al., 2017), (but see (Darnell et al., 2011), FMRP can directly bind to and regulate the translation of mRNAs encoding key actin cytoskeletal proteins, including cofilin1 (cof1) (Feuge et al., 2019), profilin1 (PFN1) (Michaelsen-Preusse et al., 2016), members of the WAVE1 complex and more (Ascano et al., 2012). Cytoplasmic FMRP interacting protein 1 (CYFIP1) is a key interacting partner of FMRP which regulates its involvement in both local translation and actin polymerization (Napoli et al., 2008). Interestingly, knockdown of FMRP has been shown to reduce the ‘ masking’ of β-actin mRNA from the translation machinery perhaps via interaction with other RNA-binding proteins like zipcode-binding protein (ZBP1) that are known to directly bind β-actin mRNA (Buxbaum et al., 2014). Our data are consistent with a model wherein presynaptic FMRP controls the localization and translation of key modulators of the actin cytoskeleton (Michaelsen-Preusse et al., 2018) and/or indirectly modulates the translatability of β-actin mRNA itself. FMRP also has non-translational functions as well, including binding to and regulating ion channel activation (Brown et al., 2010; Deng et al., 2019; Yang et al., 2018; Zhang et al., 2012). Because our study used a conditional KO strategy to remove FMRP specifically from GCs after P21, we can distinguish the role of FMRP in activity-dependent plasticity at mature synapses from its involvement in early development of MF synapses.

Previous studies have suggested that FMRP granules are dynamically regulated by phosphorylation. Dephosphorylation of FMRP is associated with granule disassembly and translational activation (Narayanan et al., 2007) whereas phosphorylation is linked to assembled, translationally-silenced granules (Tsang et al., 2019). We demonstrate that granule assembly and disassembly is regulated by activity in presynaptic MFBs. Our data also indicate that PKA activation increases protein synthesis and decreases phospho-FMRP levels, consistent with granule disassembly (Muddashetty et al., 2011; Narayanan et al., 2007; Tsang et al., 2019), in a PP2A-dependent manner. Moreover, PP2A is required for MF-LTP. These results also suggest that LTP-induced protein synthesis relies on the molecular expression mechanism of MF-LTP, not just changes in GC activity. Given that PKA activation has been shown to activate PP2A in vitro and in brain slices (Ahn et al., 2007), we propose that LTP-induced PKA activation triggers PP2A-mediated dephosphorylation of FMRP in MFBs leading to activity-dependent protein synthesis (Figure 7; Supp. Figure 5).

Our data show cKO of FMRP from presynaptic GCs increased protein synthesis in MFBs, but we failed to detect changes in basal MFB volume. Protein synthesis was further increased following LTP in *Fmr1* cKOs and cKO prevented the expression of structural and functional LTP. These observations indicate that the protein synthesis rate does not predict the size of the MFB and that loss of presynaptic FMRP does not prevent increases in total protein synthesis upon activity. Redundant mechanisms likely exist to ensure activity-induced protein synthesis. The impairment in structural and functional LTP we observed in *Fmr1* cKO mice could result from the uncontrolled enhancement of protein synthesis which

may disturb the activity-dependent increases of specific proteins necessary for plasticity or cause the unchecked synthesis of a putative negative regulator of presynaptic function that may be normally suppressed during LTP. FMRP likely directs an activity-dependent cascade responsible for tailoring MFB volume to the precise demands of the synapse via axonal targeting and translational control of a *specific subset* of mRNAs (Antar and Bassell, 2003). This interpretation is consistent with many previous studies suggesting that LTP expression depends on the precise control of the amount of protein synthesized locally, as well as the proper distribution of mRNA species (Sutton and Schuman, 2006). Dysregulated presynaptic protein synthesis and impaired long-term presynaptic plasticity could contribute to the pathophysiology of FXS and other ASDs (Lin et al., 2021). Future studies are warranted to address the identity of proteins synthesized locally under basal conditions and upon activity-- and how these proteins are altered by loss of presynaptic FMRP.

Significance of local protein synthesis to in vivo MF function

Due to its sparse firing pattern, the DG is ideally suited for its proposed function of pattern separation by orthogonalizing information coming from the entorhinal cortex (Treves et al., 2008). The MF-CA3 synapse is thought to initiate storage of new information while a direct projection from the entorhinal cortex to CA3 pyramidal cells may serve to initiate retrieval of previously stored representations (Treves et al., 2008). Studies of rodents exposed to different habitats, in vivo LTP (Escobar et al., 1997), or to spatial learning tasks show expansion of the infrapyramidal bundle (Routtenberg, 2010), consistent with our EE data (Supp. Figure 6D). While most of these studies focused on changes in the gross anatomical features of the MF projection, the microscale structural changes like the LTP-associated MFB enlargement we observed may respresent the fine-tuned establishment and encoding of new representations in the hippocampal circuit. Lastly, given that the subgranular zone is a neurogenic niche, and adult born GCs establish new connections in the mature brain, local presynaptic protein synthesis may be especially critical in the functional integration and pathfinding of immature MF synapses (Toni and Schinder, 2015). Future studies should examine structural plasticity and the levels and identity of newly synthesized proteins selectively at adult-born MF-CA3 synapse.

STAR Methods

Resource Availability

Lead Contact—Further information and requests for resources and reagents should be directed to and will be fulfilled by the Lead Contact, Pablo E. Castillo (pablo.castillo@einsteinmed.edu).

Materials Availability—All plasmids generated in this study are available from the Lead Contact without restriction. Reagents used in the study were of general use and from commercial sources. The plasmids generated in this study have been deposited to Addgene [p323-hySyn-Halo-mFMRP-Wpre; ID: 185909].

Data and Code Availability

- All data reported in this paper will be shared by the lead contact upon reasonable request.
- This paper does not report original code.
- Any additional information required to reanalyze the data reported in this work paper is available from the Lead Contact upon request.

Experimental Model and Subject Details

Mice were group housed in a standard 12 hr light/12 hr dark cycle. Experimental procedures adhered to NIH and Albert Einstein College of Medicine Institutional Animal Care and Use Committee guidelines. Acute transverse slices were prepared from male and female mice (P21–45): C57 BL/6J (Charles River), *Fmr1*$^{fl/fl}$ mice (Dr. David Nelson, FRAXA), RiboTag mice (Dr. Mary Kay Lobo, University of Maryland, Baltimore County). No differences were found between male and female mice so data from both sexes were combined.

Method Details

Plasmids and Lentiviral Production—High-titer lentiviruses were produced in the Einstein Genetic Engineering and Gene Therapy core according to standard protocol. Titer was quantified using fluorescence and ELISA. HaloTag-bActinCDS-bActinUTR-MS2V5 was created in the Singer lab (Addgene plasmid # 102718; http://n2t.net/addgene:102718; RRID:Addgene_102718) and is described in Halo-actin section below and previously (Yoon et al., 2016). Mouse Halo-FMRP construct was generated by replacing the EGFP with the HaloTag coding sequence in the p-EGFP-C1-Flag-mFmr1(wt) vector which was a gift from Stephanie Ceman (Addgene plasmid #87929; http://n2t.net/addgene:87929; RRID:Addgene_87929). The coding sequence of Halo-FMRP was then inserted into the multicloning site of a third generation lentivirus expression vector under the control of the human Synapsin promoter. C1QL2-ChiEFtom2A-GFP or C1QL2-ChiEFtom2A-Cre plasmids were a gift of Drs. Gaël Barthet and Christophe Mulle, Université de Bordeaux, and lentiviruses were made at the Einstein Genetic Engineering and Gene Therapy Core.

Slice Preparation and Electrophysiology—Acute transverse slices were prepared as follows: briefly, mice were decapitated, and brains were removed quickly and put into ice cold sucrose cutting solution or NMDG cutting solution. The sucrose cutting solution contained (in mM): 215 sucrose, 20 glucose, 26 $NaHCO_3$, 4 $MgCl_2$, 4 $MgSO_4$, 1.6 NaH_2PO_4, 2.5 KCl, and 1 $CaCl_2$. The NMDG cutting solution contained (in mM): 93 N-Methyl-d-glucamin, 2.5 KCl, 1.25 NaH_2PO_4, 30 $NaHCO_3$, 20 HEPES, 25 D-glucose, 2 Thiourea, 5 Na-Ascorbate, 3 Na-Pyruvate, 0.5 $CaCl_2$, 10 $MgCl_2$. Mice over P35 were cut in NMDG. The hippocampi were isolated and cut using a VT1200s microsclicer (Leica Microsystems Co.) at a thickness of 300 μm. These slices were then transferred to 32°C ACSF for 30 min and then kept at room temperature (RT) for at least 1h before recording. The artificial cerebral spinal fluid (ACSF) recording solution contained (in mM): 124 NaCl, 26 $NaHCO_3$, 10 glucose, 2.5 KCl, 1 NaH_2PO_4, 2.5 $CaCl_2$, and 1.3 $MgSO_4$. Mice under P35 were cut in sucrose solution. After ice-cold cutting, slices recovered at RT (in 50% sucrose, 50% ACSF) for <30 min and then at RT for 1 hr in ACSF. All solutions were bubbled with

95% O_2 and 5% CO_2 for at least 30 min. All experiments in acute slices and recordings were performed at 25.5 ± 0.1°C.

For extracellular field recordings, two borosilicate glass stimulating pipettes filled with ACSF were placed in the dentate GC layer at the border of the hilus and a glass recording pipette filled with 1M NaCl was placed in CA3 in stratum lucidum. To elicit synaptic responses, paired, monopolar square-wave voltage or current pulses (100–200 μs pulse width) were delivered through a stimulus isolator (Isoflex, AMPI) connected to a broken tip (~10–20 μm) stimulating patch-type micropipette filled with ACSF. Stimulus intensity was adjusted to give comparable magnitude synaptic responses across experiments (~0.2–0.6 mV). Baseline and post-induction LTP synaptic responses were monitored at 0.05 Hz. Stimulation and acquisition were controlled with IgorPro 7 (Wavemetrics). Shaded boxes in figures correspond to when plasticity was analyzed with respect to baseline and when representative traces were collected and averaged. Summary data (i.e. time-course plots and bar graphs) are presented as mean ± standard error of mean (SEM). LTP was triggered by delivering 125 pulses (25 Hz, 3X) in the presence of d-APV (Ben-Simon et al., 2015; Castillo et al., 2002; Kaeser-Woo et al., 2013). At the end of all recordings 1 μM DCG-IV was added to confirm the recording was from a MF synapse. Only recordings displaying >80% reduction in transmission following DCG-IV application were included.

For recordings in Figure 6, P21–24 *Fmr1*$^{fl/fl}$ mice were injected with an AAV encoding CAMKII-mCherry or CAMKII-mCherry-Cre into the DG using established coordinates (−2.2 posterior to Bregma, 2.0 laterally, and 2.0 ventral from dura) and a total volume of 0.5 μL/ hemisphere at a flow rate of 0.1 μL/min obtained from UNC Vector Core. 2 weeks after injection, acute hippocampal slices were made as described above. After slicing in NMDG, slices were checked for expression using epifluorescence, and excluded if any cells in CA3 were infected. LTP was induced as described above using electrical stimulation. Slices were fixed after recording and saved for post-hoc immunohistochemistry (anti-FMRP, 1:10, FRAXA) to confirm KO of FMRP (Supp. Figure 4).

Halo-actin—WT C57BL/6J mice were stereotactically injected with high titer Halo-actin lentivirus into the DG between P21-P24 using established coordinates (−2.2 posterior to Bregma, 2.0 laterally, and 2.0 ventral from dura) with a total volume of 1.5 μL/ hemisphere at a flow rate of 0.2 μL/min. The Halo-actin reporter construct includes FLAG-tag and HaloTag sequences upstream and in-frame of the β-actin coding sequence followed by the 3′ UTR of β-actin and the nonrepetitive MBSV5 aptamers. After 2–3 weeks of recovery, mice were sacrificed and acute hippocampal slices were prepared as described above. For the detection of newly translated proteins, cell-permeable Halo-ligand conjugated to a tetraalkylrhodamine derivatives (JF549-HTL and JF646HTL; Janelia Research Campus, Ashburn, VA,USA) were bath-applied in a pulse-chase assay. Slices were labelled with JF549-HTL (100 nM) in ACSF in a chamber oxygenated with 95% O_2/5% CO_2 for 1 hour to label all the preexisting Halo-actin, then washed out in ACSF for 30 minutes. Next, JF646-HTL (200 nM) was bath-applied to label newly synthesized Halo-actin, then washed out for 30 min in ACSF. For some controls, the order of the dyes was reversed. The translation inhibitor CHX (80 μM; Tocris) were added to the pulse and included in all subsequent steps until the last washout step before imaging in some experiments. LTP was

induced in a subset of slices using electrical stimulation with 2 glass pipettes in the DG, as described in the section on electrophysiology, in the presence of d-APV.

For experiments involving photo-activation, bath-application of PA-JF646 was performed as described above at 2 time intervals (Figure 2). White light from the Sola Lumencor light engine (Lumencor) was directed through a 40X objective to focus the photoactivation on an ~ 200 μm diameter circle of the acute hippocampal slice. To activate, a mirror was used to reflect the full light spectrum of the laser at the tissue for 1 s. The slices were fixed with 4% PFA, mounted and imaged on a Zeiss LSM 880 with Airyscan using a Plan-Apochromat 63X/1.4 Oil DIC M27 and 1.8X zoom. Images were Airyscan processed prior to analysis. Threshold, laser power, and gain were kept constant for each experiment. Pixel width and height was 0.049 μm and voxel depth was 0.187 μm. Z-stacks were taken throughout stratum lucidum at similar depths such that boutons were captured in their entirety (i.e. not cut off). Tiled fluorescence images were obtained with a Plan-Apochromat 10X/0.45 M27 objective with 1.8X zoom. Analysis was performed using FIJI by hand-drawing an ROI around MFBs based on the pre-existing actin channel, JF-549 or Halo-tag antibody (1:500, Promega, mouse monoclonal, RRID: AB_713650) and measuring the newly synthesized actin (in most cases, JF-646) within this ROI. Filopodia were identified by a trained, blind experimenter as thin protrusions from the main bouton greater than 0.5 μm in length.

Immunohistochemistry—Slices were washed twice in 1XPBS then incubated in blocking buffer (4% goat serum in 1XPBS + 2% BSA + 0.1% Tx-100) for 1 hr at RT. Primary antibodies were diluted directly into the antibody buffer (blocking buffer without goat serum) and floating slices were incubated overnight at 4°C. After 4 washes with 1XPBS, slices were incubated in secondary antibodies (Invitrogen, Carlsbad, CA, USA; RRID: AB_2535812, RRID: AB_2633277, RRID: AB_144696, RRID: AB_143165) diluted in blocking buffer overnight at 4°C. Slices were washed 5X with 1XPBS, then mounted.

MF Bouton Structural Analysis—*Fmr1*$^{fl/fl}$ mice (Figure 6) and WT C57BL/6J (Figure 5) were stereotactically injected with high titer lentiviral constructs (C1QL2-ChiEFtom2A-GFP or C1QL2-ChiEFtom2A-Cre) into the DG between P21-P24 using established coordinates (−2.2 posterior to Bregma, 2.0 laterally, and 2.0 ventral from dura) using a total volume of 2 μL/ hemisphere at a flow rate of 0.2 μL/min. 2–3 weeks after injection, 300 μm acute hippocampal slices were prepared as described above. LTP was induced using optogenetics in some experiments. Briefly, pulses of blue light were provided with a 473 nm wavelength laser (OEM laser systems Inc., ~ 25 mw/mm power) aimed at the hilus of slices using an optic fiber (200 μm diameter), collimated and delivered through the microscope objective (40X, 0.8 NA) in a submerged chamber with oxygenated ACSF flowing. Cycloheximide (CHX, 80 μM) was added to the bath for conditions indicated in Figure 5. An LTP protocol (125 pulses, 25 Hz, 3X) was delivered in the presence of d-APV using light pulses of 1 ms duration. Slices were incubated at RT for 1 hr after delivering the LTP protocol in oxygenated ACSF before overnight fixation in 4% PFA in 1XPBS. Slices were rinsed and mounted, except for a few controls that were also processed for immunohistochemistry to confirm MF bouton localization. tdTomato-ChiEF fluorescent signal was imaged with 561 nm laser to measure bouton structure. Images were acquired

on a Zeiss LSM 880 with Airyscan using a Plan-Apochromat 63X/1.4 Oil DIC M27 and 1.8X zoom. Images were Airyscan processed prior to analysis. Threshold, laser power, and gain were kept constant for each experiment. Pixel width and height was 0.049 μm and voxel depth was 0.187 μm. Z-stacks were taken throughout stratum lucidum at similar depths in order to control for PFA permeation. Imaris 9.2 software was used to reconstruct boutons in 3D using the Surface function. MFBs were individually screened and compared with the z-stack after 3D reconstruction to ensure correct identification. Only boutons that were greater than 5 μm^3 and did not touch the image border were included. For filopodial analysis, z-stacks were maximum projected in FIJI and all protrusions having greater than 0.3 μm displacement from the main bouton and not visibly connected to an axon were considered, then a line was drawn down the filopodia starting at the middle touching the bouton surface to measure length in 2D. For consistency, filopodial analysis was performed by the same person for all conditions, separate from the person that did imaging. All imaging and analysis was performed blind to treatment group.

Puromycylation—*Fmr1*$^{fl/fl}$ mice were injected with an AAV encoding CAMKII-mCherry or CAMKII-mCherry-Cre into the DG using established coordinates (−2.2 posterior to Bregma, 2.0 laterally, and 2.0 ventral from dura) and a total volume of 0.5 μL/ hemisphere at a flow rate of 0.1 μL/min obtained from UNC Vector Core, identical to conditions used for electrophysiological recordings. For all EE experiments, animals were exposed 1 day after stereotaxic injection for 2 weeks (*see* enriched environment *section for details*). Acute slices were cut as described in the Slice Preparation and Electrophysiological Recording section 2 weeks after stereotaxic injection and were checked for expression using epifluorescence and were excluded if any cells in CA3 were infected. Puromycin dihydrochloride was diluted into ACSF from a stock of 50 mM. Slices were incubated with puromycin (50 μM) for 15 min, then LTP was induced using electrical stimulation in the DG in the presence of d-APV, and slices were incubated for 15 more minutes after LTP induction. For experiments using synaptic blockers: NBQX, 5 μM; d-APV, 50 μM; MPEP, 4 μM; YM298198, 50 μM were added to slices for the first 15 minutes of puromycin incubation and during LTP. After LTP, slices were returned to ACSF + puromycin for 15 more minutes. For CHX and anisomycin controls (80 or 30 μM respectively), slices were pre-incubated in protein synthesis inhibitors for 25 minutes before puromycin incubation. For FSK, slices were incubated in puromycin for 10 minutes, FSK and puromycin for 10 minutes and then back in ACSF + puromycin for 10 minutes. For experiments using okadaic acid, slices were pre-treated with okadaic acid + puromycin for 30 min prior to and during LTP induction. Slices were then fixed for 1 hr in 4% PFA, blocked for 30 minutes, and stained according to the immunohistochemistry protocol above (primary antibodies: anti-ZnT3, rabbit polyclonal, 1:500, Synaptic Systems, RRID: AB_10894885; anti-puromycin 1:1000, EMD Millipore, RRID: AB_2566826) and imaged on the Zeiss LSM 880 with Airyscan using a LD LCI Plan-Apochromat 25X/0.8 mm Korr DIC M27and 1.8X zoom. Images were Airyscan processed prior to analysis. Quantification was perfomed using FIJI by drawing regions of interest in the ZnT3 channel in which puromycin fluorescence intensity was measured in stratum lucidum. For stratum radiatum control, puromycin signal in regions of interest distal to the stratum lucidum as indicated by the ZnT3 labeling were measured.

Halo-FMRP—WT C57BL/6J mice were stereotactically injected with high titer Halo-FMRP lentivirus into the DG between P21-P24 using established coordinates (−2.2 posterior to Bregma, 2.0 laterally, and 2.0 ventral from dura) using a total volume of 1.5 μL/hemisphere at a flow rate of 0.2 μL/min. After 2–3 weeks of recovery, mice were sacrificed and acute hippocampal slices were prepared as described above. For the detection of Halo-FMRP, cell-permeable Halo-ligand conjugated to a tetraalkylrhodamine derivative (JF549-HTL), numbers indicate wavelength of excitation) was bath-applied in a pulse-chase assay. Slices were labelled with JF549-HTL (100 nM) in ACSF in a chamber oxygenated with 95%O2/5% CO_2 for 1 hour to label all Halo-FMRP. For LTP experiments, electrical LTP was triggered using two borosilicate glass stimulating micropipettes with a broken tip ~ 20 μm filled with ACSF placed in the dentate GC layer at the border of the hilus, and MF-LTP protocol was delivered as described above. For chemical induction of LTP, forskolin (50 μM) was bath applied for 10 minutes. For control experiments using okadaic acid, slices were pre-treated with okadaic acid for 30 min prior to and during LTP induction, as above. 15 minutes after the start of electrical or chemical LTP induction slices were fixed with 4% PFA and mounted. Images were acquired on a Zeiss LSM 880 with Airyscan using a Plan-Apochromat 63X/1.4 Oil DIC M27 and 1.8X zoom. Images were Airyscan processed prior to analysis. Threshold, laser power, and gain were kept constant for each experiment. Z-stacks of identical size were taken at similar depths were maximum projected. Analysis was performed on high-resolution images of MFBs using FIJI ‘ Analyze particles’ with 2 different parameter sets: one to capture only high intensity puncta of diameter 0.25–1 μm^2 (assembled granules) and another to capture diffuse low intensity regions within MFBs between 3 – 30 μm^2 (disassembled granules).

For controls in Supp. Figure 5A, dissociated hippocampal neurons in culture were infected with Halo-FMRP at DIV9 and fixed at DIV14. Immunofluorescence was performed using monoclonal FMRP antibody 7G1 (deposited by Warren, S.T. to the Developmental Studies Hybridoma Bank at the University of Iowa, Iowa City, IA, USA) at 1:10 dilution and polyclonal HaloTag antibody (Promega Corp. Madison, WI, USA) at 1:500 dilution and FITC-conjugated donkey anti-mouse secondary antibody and Cy3-conjugated goat anti-rabbit secondary antibody (Invitrogen; 1:1000).

pFMRP (Ser499) Staining—Acute hippocampal slices were cut from WT C57BL/6J mice as described in the Slice Preparation and Electrophysiological Recording section. For chemical induction of LTP, forskolin (50 μM) was bath applied for 10 minutes. For control experiments using okadaic acid, slices were pre-treated with okadaic acid for 30 min prior to and during FSK-LTP induction. 10 minutes after the end of FSK-LTPinduction slices were fixed with 4% PFA, stained with anti-FMRP (Ser499) antibody (1:200, PhosphoSolutions, RRID: AB_2492094) and mounted. Images were acquired on a Zeiss LSM 880 with Airyscan using a Plan-Apochromat 25X/0.8 mm Korr DIC M27and 1.8X zoom. Images were Airyscan processed prior to analysis. Laser power, and gain were kept constant for each experiment. Z-stacks of identical size were taken at similar depths were maximum projected. Analysis was performed on high-resolution images of GCs using FIJI.

RiboTag—RiboTag mice were injected with C1QL2-ChiEFtom2A-GFP or C1QL2-ChiEFtom2A-Cre at age P21 and sacrificed after 3 weeks. Animals were transcardially perfused with 4% PFA in 0.1M 1XPBS. After 48h fixation in 4% PFA, 125 μm-thick brain coronal sections were prepared using a DSK Microslicer (DTK-1000). Brain slices were kept in 1XPBS until staining as described above in Immunohistochemistry using Rb pAb to HA tag (1:1000, Abcam ab9110, RRID: AB_307019). For image quantification in FIJI after Airyscan processing, Z-stacks of identical size were taken at similar depths and maximally projected. Quantification was perfomed by drawing regions of interest in the TdTomato labeled MFBs channel in which HA signal that was overlapping was measured.

Enriched Environment—Home cages (HCs) are standard mouse cages with single housed mice. Their dimensions are 28 cm (11”) × 18 cm (7”), and they have a wire feeder lid and a water bottle. Mice assigned to enriched environment (EE) housing are kept in groups of at least 5 in a large 121 cm (4 ft) × 61 cm (2 ft) enriched cage, containing a feeder, water dispenser, several running wheels, as well as plastic tubes, domes and other structures (Supp. Figure 5A). Objects are rearranged every other day to maintain novelty. Female and male mice are never mixed in the same cage, and all males are housed with littermates. EE refers to both the effects of enrichment strictly defined (exploration, novel objects, increased area), as well as the exercise associated with exploration of the environment, and the use of running wheels. For all EE experiments, one HC and one EE mouse was cut per day, and experimenters were blind to condition for imaging and analysis. Experiments to quantify structure, puromycin labeling, and Halo-actin expression were all performed as described above.

Reagents—Stock reagents were prepared according to the manufacturer’s recommendation in water, DMSO (<0.01% final volume during experiments), or phosphate buffered saline (PBS), stored at −20°C, and diluted into ACSF or intracellular recording solutions as needed. d-APV was acquired from the NIMH Chemical Synthesis and Drug Supply Program; salts for making cutting solutions, ACSF, puromycin dihydrochloride and DCG-IV from Sigma Aldrich (St. Louis, MO, USA); CHX, MPEP and YM298198 from Tocris Bioscience (Bristol, UK), anisomycin from ALFA Aesar (Ward Hill, MA, USA), okadaic acid and NBQX from Cayman Chemical (Ann Arbor, MI, USA). Reagents were either acutely bath applied or preincubated with slices/cultures, as indicated in Results.

Experimental Design—All experiments were performed in an interleaved fashion and include at least 3 mice and multiple technical replicates. Experimenters were blind to genotype during recording/imaging and analysis. Sample size was estimated using power analysis.

Quantification and Statistical Analysis

Analysis and statistics were carried out in OriginPro 2015 (OriginLab) and Graphpad Prism 8. Significance ($p < 0.05$) was assessed with one-way ANOVA (means comparison with *post hoc* Bonferroni test), Student’s paired and unpaired t-tests, Wilcoxon matched-pairs signed rank test, Mann Whitney test, Pearson’s correlation coefficient,or Two-Way ANOVA with post-hoc Tukey’s test as indicated. Normality tests were used to determine the use of

parametric or nonparametric tests. Statistical parameters including exact value of ‘ n’ and what ‘ n’ represents are reported in the figured legends. Python 3.0 was used to generate Superplots in structural plasticity figures.

Supplementary Material

Refer to Web version on PubMed Central for supplementary material.

Acknowledgements:

We thank all Castillo Lab and Singer Lab members, and Dr. Benjamin Hobson for helpful discussions. We thank Dr. Kostantin Dobrenis, Kevin Fisher, and Vladimir Mudragel of the Einstein Neural Cell Engineering and Imaging Core (supported by The Rose F. Kennedy Intellectual Disabilities Research Center) for their advice and assistance with imageacquisition and analysis. We thank Dr. Stefano Lutzu for whole-cell recordings (Supp. Figure 6C). We are grateful to Dr. Mary Kay Lobo University of Maryland, Baltimore County for donating the Ribotag mice, Drs. Gael Barthet and Christophe Mulle, Universite de Bordeaux, for sharing the C1ql2 constructs, the FRAXA foundation for the *Fmr1*$^{fl/fl}$ mouse line, and the Lavis Lab for the JF dyes. This research was supported by the National Institutes of Health: F31MH114431 to HRM; R01-MH125772, R01-NS113600, R01-NS11543, R01-MH116673, and a pilot grant through NICHD U54 HD090260 to PEC; R01-NS083085 to RHS, R21-MH120496 to YJY; R01-NS083085 to RHS, and a shared instrument grant (S10OD025295) to Konstantin Dobrenis.

References:

Acsady L, and Kali S (2007). Models, structure, function: the transformation of cortical signals in the dentate gyrus. Prog Brain Res 163, 577–599. 10.1016/S0079-6123(07)63031-3. [PubMed: 17765739]

Acsady L, Kamondi A, Sik A, Freund T, and Buzsaki G (1998). GABAergic cells are the major postsynaptic targets of mossy fibers in the rat hippocampus. J Neurosci 18, 3386–3403. [PubMed: 9547246]

Ahn JH, McAvoy T, Rakhilin SV, Nishi A, Greengard P, and Nairn AC (2007). Protein kinase A activates protein phosphatase 2A by phosphorylation of the B56delta subunit. Proc Natl Acad Sci U S A 104, 2979–2984. 10.1073/pnas.0611532104. [PubMed: 17301223]

Akins MR, Berk-Rauch HE, Kwan KY, Mitchell ME, Shepard KA, Korsak LI, Stackpole EE, Warner-Schmidt JL, Sestan N, Cameron HA, and Fallon JR (2017). Axonal ribosomes and mRNAs associate with fragile X granules in adult rodent and human brains. Hum Mol Genet 26, 192–209. 10.1093/hmg/ddw381. [PubMed: 28082376]

Antar LN, and Bassell GJ (2003). Sunrise at the synapse: the FMRP mRNP shaping the synaptic interface. Neuron 37, 555–558. [PubMed: 12597853]

Antar LN, Dictenberg JB, Plociniak M, Afroz R, and Bassell GJ (2005). Localization of FMRP-associated mRNA granules and requirement of microtubules for activity-dependent trafficking in hippocampal neurons. Genes, brain, and behavior 4, 350–359. 10.1111/j.1601-183X.2005.00128.×. [PubMed: 16098134]

Ascano M Jr., Mukherjee N, Bandaru P, Miller JB, Nusbaum JD, Corcoran DL, Langlois C, Munschauer M, Dewell S, Hafner M, et al. (2012). FMRP targets distinct mRNA sequence elements to regulate protein expression. Nature 492, 382–386. 10.1038/nature11737. [PubMed: 23235829]

Bagni C, and Zukin RS (2019). A Synaptic Perspective of Fragile X Syndrome and Autism Spectrum Disorders. Neuron 101, 1070–1088. 10.1016/j.neuron.2019.02.041. [PubMed: 30897358]

Bailey CH, Kandel ER, and Harris KM (2015). Structural Components of Synaptic Plasticity and Memory Consolidation. Cold Spring Harb Perspect Biol 7, a021758. 10.1101/cshperspect.a021758. [PubMed: 26134321]

Barnes SJ, Opitz T, Merkens M, Kelly T, von der Brelie C, Krueppel R, and Beck H (2010). Stable mossy fiber long-term potentiation requires calcium influx at the granule cell soma, protein synthesis, and microtubule-dependent axonal transport. J Neurosci 30, 12996–13004. 10.1523/JNeUrOSCI.1847-10.2010. [PubMed: 20881117]

Barthet G, Jorda-Siquier T, Rumi-Masante J, Bernadou F, Muller U, and Mulle C (2018). Presenilin-mediated cleavage of APP regulates synaptotagmin-7 and presynaptic plasticity. Nat Commun 9, 4780. 10.1038/s41467-018-06813-x. [PubMed: 30429473]

Ben-Simon Y, Rodenas-Ruano A, Alvina K, Lam AD, Stuenkel EL, Castillo PE, and Ashery U (2015). A Combined Optogenetic-Knockdown Strategy Reveals a Major Role of Tomosyn in Mossy Fiber Synaptic Plasticity. Cell reports 12, 396–404. 10.1016/j.celrep.2015.06.037. [PubMed: 26166572]

Bourgeron T (2015). From the genetic architecture to synaptic plasticity in autism spectrum disorder. Nat Rev Neurosci 16, 551–563. 10.1038/nrn3992. [PubMed: 26289574]

Brown MR, Kronengold J, Gazula VR, Chen Y, Strumbos JG, Sigworth FJ, Navaratnam D, and Kaczmarek LK (2010). Fragile X mental retardation protein controls gating of the sodium-activated potassium channel Slack. Nat Neurosci 13, 819–821. 10.1038/nn.2563. [PubMed: 20512134]

Brown V, Jin P, Ceman S, Darnell JC, O'Donnell WT, Tenenbaum SA, Jin X, Feng Y, Wilkinson KD, Keene JD, et al. (2001). Microarray identification of FMRP-associated brain mRNAs and altered mRNA translational profiles in fragile X syndrome. Cell 107, 477–487. [PubMed: 11719188]

Buxbaum AR, Wu B, and Singer RH (2014). Single beta-actin mRNA detection in neurons reveals a mechanism for regulating its translatability. Science 343, 419–422. 10.1126/science.1242939. [PubMed: 24458642]

Cajigas IJ, Tushev G, Will TJ, tom Dieck S, Fuerst N, and Schuman EM (2012). The local transcriptome in the synaptic neuropil revealed by deep sequencing and high-resolution imaging. Neuron 74, 453–466. 10.1016/j.neuron.2012.02.036. [PubMed: 22578497]

Calixto E, Thiels E, Klann E, and Barrionuevo G (2003). Early maintenance of hippocampal mossy fiber--long-term potentiation depends on protein and RNA synthesis and presynaptic granule cell integrity. J Neurosci 23, 4842–4849. [PubMed: 12832506]

Caroni P, Donato F, and Muller D (2012). Structural plasticity upon learning: regulation and functions. Nat Rev Neurosci 13, 478–490. 10.1038/nrn3258. [PubMed: 22714019]

Castillo PE (2012). Presynaptic LTP and LTD of excitatory and inhibitory synapses. Cold Spring Harb Perspect Biol 4. 10.1101/cshperspect.a005728.

Castillo PE, Schoch S, Schmitz F, Sudhof TC, and Malenka RC (2002). RIM1alpha is required for presynaptic long-term potentiation. Nature 415, 327–330. 10.1038/415327a. [PubMed: 11797010]

Chierzi S, Stachniak TJ, Trudel E, Bourque CW, and Murai KK (2012). Activity maintains structural plasticity of mossy fiber terminals in the hippocampus. Mol Cell Neurosci 50, 260–271. 10.1016/j.mcn.2012.05.004. [PubMed: 22579606]

Christie SB, Akins MR, Schwob JE, and Fallon JR (2009). The FXG: a presynaptic fragile X granule expressed in a subset of developing brain circuits. J Neurosci 29, 1514–1524. 10.1523/JNEUROSCI.3937-08.2009. [PubMed: 19193898]

Chyung E, LeBlanc HF, Fallon JR, and Akins MR (2018). Fragile X granules are a family of axonal ribonucleoprotein particles with circuit-dependent protein composition and mRNA cargos. J Comp Neurol 526, 96–108. 10.1002/cne.24321. [PubMed: 28884477]

Cingolani LA, and Goda Y (2008). Actin in action: the interplay between the actin cytoskeleton and synaptic efficacy. Nat Rev Neurosci 9, 344–356. 10.1038/nrn2373. [PubMed: 18425089]

Claiborne BJ, Amaral DG, and Cowan WM (1990). Quantitative, three-dimensional analysis of granule cell dendrites in the rat dentate gyrus. J Comp Neurol 302, 206–219. 10.1002/cne.903020203. [PubMed: 2289972]

Cohen LD, and Ziv NE (2017). Recent insights on principles of synaptic protein degradation. F1000Res 6, 675. 10.12688/f1000research.10599.1. [PubMed: 28620464]

Costa-Mattioli M, Sossin WS, Klann E, and Sonenberg N (2009). Translational control of long-lasting synaptic plasticity and memory. Neuron 61, 10–26. 10.1016/j.neuron.2008.10.055. [PubMed: 19146809]

Danzer SC, He X, Loepke AW, and McNamara JO (2010). Structural plasticity of dentate granule cell mossy fibers during the development of limbic epilepsy. Hippocampus 20, 113–124. 10.1002/hipo.20589. [PubMed: 19294647]

Darnell JC, and Klann E (2013). The translation of translational control by FMRP: therapeutic targets for FXS. Nat Neurosci 16, 1530–1536. 10.1038/nn.3379. [PubMed: 23584741]

Darnell JC, Van Driesche SJ, Zhang C, Hung KY, Mele A, Fraser CE, Stone EF, Chen C, Fak JJ, Chi SW, et al. (2011). FMRP stalls ribosomal translocation on mRNAs linked to synaptic function and autism. Cell 146, 247–261. 10.1016/j.cell.2011.06.013. [PubMed: 21784246]

David A, Dolan BP, Hickman HD, Knowlton JJ, Clavarino G, Pierre P, Bennink JR, and Yewdell JW (2012). Nuclear translation visualized by ribosome-bound nascent chain puromycylation. J Cell Biol 197, 45–57. 10.1083/jcb.201112145. [PubMed: 22472439]

De Paola V, Arber S, and Caroni P (2003). AMPA receptors regulate dynamic equilibrium of presynaptic terminals in mature hippocampal networks. Nat Neurosci 6, 491–500. 10.1038/nn1046. [PubMed: 12692557]

Deng PY, Carlin D, Oh YM, Myrick LK, Warren ST, Cavalli V, and Klyachko VA (2019). Voltage-Independent SK-Channel Dysfunction Causes Neuronal Hyperexcitability in the Hippocampus of Fmr1 Knock-Out Mice. J Neurosci 39, 28–43. 10.1523/JNEUROSCI.1593-18.2018. [PubMed: 30389838]

Deng PY, Sojka D, and Klyachko VA (2011). Abnormal presynaptic short-term plasticity and information processing in a mouse model of fragile X syndrome. J Neurosci 31, 10971–10982. 10.1523/JNEUROSCI.2021-11.2011. [PubMed: 21795546]

Diamantaki M, Frey M, Berens P, Preston-Ferrer P, and Burgalossi A (2016). Sparse activity of identified dentate granule cells during spatial exploration. Elife 5. 10.7554/eLife.20252.

Dictenberg JB, Swanger SA, Antar LN, Singer RH, and Bassell GJ (2008). A direct role for FMRP in activity-dependent dendritic mRNA transport links filopodial-spine morphogenesis to fragile X syndrome. Developmental cell 14, 926–939. 10.1016/j.devcel.2008.04.003. [PubMed: 18539120]

Eliscovich C, Shenoy SM, and Singer RH (2017). Imaging mRNA and protein interactions within neurons. Proc Natl Acad Sci U S A 114, E1875–E1884. 10.1073/pnas.1621440114. [PubMed: 28223507]

Escobar ML, Barea-Rodriguez EJ, Derrick BE, Reyes JA, and Martinez JL Jr. (1997). Opioid receptor modulation of mossy fiber synaptogenesis: independence from long-term potentiation. Brain Res 751, 330–335. 10.1016/s0006-8993(96)01373-x. [PubMed: 9099823]

Evstratova A, and Toth K (2014). Information processing and synaptic plasticity at hippocampal mossy fiber terminals. Front Cell Neurosci 8, 28. 10.3389/fncel.2014.00028. [PubMed: 24550783]

Feuge J, Scharkowski F, Michaelsen-Preusse K, and Korte M (2019). FMRP Modulates Activity-Dependent Spine Plasticity by Binding Cofilin1 mRNA and Regulating Localization and Local Translation. Cereb Cortex 29, 5204–5216. 10.1093/cercor/bhz059. [PubMed: 30953439]

Galimberti I, Gogolla N, Alberi S, Santos AF, Muller D, and Caroni P (2006). Long-term rearrangements of hippocampal mossy fiber terminal connectivity in the adult regulated by experience. Neuron 50, 749–763. 10.1016/j.neuron.2006.04.026. [PubMed: 16731513]

Gogolla N, Galimberti I, and Caroni P (2007). Structural plasticity of axon terminals in the adult. Curr Opin Neurobiol 17, 516–524. 10.1016/j.conb.2007.09.002. [PubMed: 17950593]

Gogolla N, Galimberti I, Deguchi Y, and Caroni P (2009). Wnt signaling mediates experience-related regulation of synapse numbers and mossy fiber connectivities in the adult hippocampus. Neuron 62, 510–525. 10.1016/j.neuron.2009.04.022. [PubMed: 19477153]

Grimm JB, English BP, Chen J, Slaughter JP, Zhang Z, Revyakin A, Patel R, Macklin JJ, Normanno D, Singer RH, et al. (2015). A general method to improve fluorophores for live-cell and single-molecule microscopy. Nat Methods 12, 244–250, 243 p following 250. 10.1038/nmeth.3256. [PubMed: 25599551]

Grimm JB, English BP, Choi H, Muthusamy AK, Mehl BP, Dong P, Brown TA, Lippincott-Schwartz J, Liu Z, Lionnet T, and Lavis LD (2016). Bright photoactivatable fluorophores for single-molecule imaging. Nat Methods 13, 985–988. 10.1038/nmeth.4034. [PubMed: 27776112]

Grollman AP (1967). Inhibitors of protein biosynthesis. II. Mode of action of anisomycin. J Biol Chem 242, 3226–3233. [PubMed: 6027796]

Hafner AS, Donlin-Asp PG, Leitch B, Herzog E, and Schuman EM (2019). Local protein synthesis is a ubiquitous feature of neuronal pre- and postsynaptic compartments. Science 364. 10.1126/science.aau3644.

Hagerman R, Au J, and Hagerman P (2011). FMR1 premutation and full mutation molecular mechanisms related to autism. J Neurodev Disord 3, 211–224. 10.1007/s11689-011-9084-5. [PubMed: 21617890]

Henze DA, Urban NN, and Barrionuevo G (2000). The multifarious hippocampal mossy fiber pathway: a review. Neuroscience 98, 407–427. [PubMed: 10869836]

Henze DA, Wittner L, and Buzsaki G (2002). Single granule cells reliably discharge targets in the hippocampal CA3 network in vivo. Nat Neurosci 5, 790–795. 10.1038/nn887. [PubMed: 12118256]

Holt CE, Martin KC, and Schuman EM (2019). Local translation in neurons: visualization and function. Nat Struct Mol Biol 26, 557–566. 10.1038/s41594-019-0263-5. [PubMed: 31270476]

Huang CC, and Hsu KS (2004). Local protein synthesis and GABAB receptors regulate the reversibility of long-term potentiation at murine hippocampal mossy fibre-CA3 synapses. J Physiol 561, 91–108. 10.1113/jphysiol.2004.072546. [PubMed: 15345751]

Huang YY, Li XC, and Kandel ER (1994). cAMP contributes to mossy fiber LTP by initiating both a covalently mediated early phase and macromolecular synthesis-dependent late phase. Cell 79, 69–79. [PubMed: 7923379]

Ivanco TL, and Greenough WT (2002). Altered mossy fiber distributions in adult Fmr1 (FVB) knockout mice. Hippocampus 12, 47–54. 10.1002/hipo.10004. [PubMed: 11918288]

Iwasaki S, and Ingolia NT (2017). The Growing Toolbox for Protein Synthesis Studies. Trends Biochem Sci 42, 612–624. 10.1016/j.tibs.2017.05.004. [PubMed: 28566214]

Kaeser-Woo YJ, Younts TJ, Yang X, Zhou P, Wu D, Castillo PE, and Sudhof TC (2013). Synaptotagmin-12 phosphorylation by cAMP-dependent protein kinase is essential for hippocampal mossy fiber LTP. J Neurosci 33, 9769–9780. 10.1523/JNEUROSCI.5814-12.2013. [PubMed: 23739973]

Kempermann G, Kuhn HG, and Gage FH (1997). More hippocampal neurons in adult mice living in an enriched environment. Nature 386, 493–495. 10.1038/386493a0. [PubMed: 9087407]

Klein ME, Monday H, and Jordan BA (2016). Proteostasis and RNA Binding Proteins in Synaptic Plasticity and in the Pathogenesis of Neuropsychiatric Disorders. Neural plasticity 2016, 3857934. 10.1155/2016/3857934. [PubMed: 26904297]

Koga K, Liu MG, Qiu S, Song Q, O'Den G, Chen T, and Zhuo M (2015). Impaired presynaptic long-term potentiation in the anterior cingulate cortex of Fmr1 knock-out mice. J Neurosci 35, 2033–2043. 10.1523/JNEUROSCI.2644-14.2015. [PubMed: 25653361]

Lai A, Valdez-Sinon AN, and Bassell GJ (2020). Regulation of RNA granules by FMRP and implications for neurological diseases. Traffic 21, 454–462. 10.1111/tra.12733. [PubMed: 32374065]

Lawrence JJ, Grinspan ZM, and McBain CJ (2004). Quantal transmission at mossy fibre targets in the CA3 region of the rat hippocampus. J Physiol 554, 175–193. 10.1113/jphysiol.2003.049551. [PubMed: 14678500]

Leung KM, van Horck FP, Lin AC, Allison R, Standart N, and Holt CE (2006). Asymmetrical beta-actin mRNA translation in growth cones mediates attractive turning to netrin-1. Nat Neurosci 9, 1247–1256. 10.1038/nn1775. [PubMed: 16980963]

Lin JQ, van Tartwijk FW, and Holt CE (2021). Axonal mRNA translation in neurological disorders. RNA Biol 18, 936–961. 10.1080/15476286.2020.1822638. [PubMed: 32988274]

Louros SR, and Osterweil EK (2016). Perturbed proteostasis in autism spectrum disorders. J Neurochem. 10.1111/jnc.13723.

Maruo T, Mandai K, Takai Y, and Mori M (2016). Activity-dependent alteration of the morphology of a hippocampal giant synapse. Molecular and cellular neurosciences 71, 25–33. 10.1016/j.mcn.2015.12.005. [PubMed: 26687760]

Mayford M, Siegelbaum SA, and Kandel ER (2012). Synapses and memory storage. Cold Spring Harb Perspect Biol 4. 10.1101/cshperspect.a005751.

Mazare N, Oudart M, Moulard J, Cheung G, Tortuyaux R, Mailly P, Mazaud D, Bemelmans AP, Boulay AC, Blugeon C, et al. (2020). Local Translation in Perisynaptic Astrocytic Processes Is Specific and Changes after Fear Conditioning. Cell reports 32, 108076. 10.1016/j.celrep.2020.108076. [PubMed: 32846133]

Michaelsen-Preusse K, Feuge J, and Korte M (2018). Imbalance of synaptic actin dynamics as a key to fragile X syndrome? J Physiol 596, 2773–2782. 10.1113/JP275571. [PubMed: 29380377]

Michaelsen-Preusse K, Zessin S, Grigoryan G, Scharkowski F, Feuge J, Remus A, and Korte M (2016). Neuronal profilins in health and disease: Relevance for spine plasticity and Fragile X syndrome. Proc Natl Acad Sci U S A 113, 3365–3370. 10.1073/pnas.1516697113. [PubMed: 26951674]

Mientjes EJ, Nieuwenhuizen I, Kirkpatrick L, Zu T, Hoogeveen-Westerveld M, Severijnen L, Rife M, Willemsen R, Nelson DL, and Oostra BA (2006). The generation of a conditional Fmr1 knock out mouse model to study Fmrp function in vivo. Neurobiol Dis 21, 549–555. 10.1016/j.nbd.2005.08.019. [PubMed: 16257225]

Mineur YS, Sluyter F, de Wit S, Oostra BA, and Crusio WE (2002). Behavioral and neuroanatomical characterization of the Fmr1 knockout mouse. Hippocampus 12, 39–46. 10.1002/hipo.10005. [PubMed: 11918286]

Monday HR, Bourdenx M, Jordan BA, and Castillo PE (2020). CB1 receptor-mediated inhibitory LTD triggers presynaptic remodeling via protein synthesis and ubiquitination. bioRxiv, 2020.2001.2009.900464. 10.1101/2020.01.09.900464.

Monday HR, and Castillo PE (2017). Closing the gap: long-term presynaptic plasticity in brain function and disease. Curr Opin Neurobiol 45, 106–112. 10.1016/j.conb.2017.05.011. [PubMed: 28570863]

Monday HR, Younts TJ, and Castillo PE (2018). Long-Term Plasticity of Neurotransmitter Release: Emerging Mechanisms and Contributions to Brain Function and Disease. Annu Rev Neurosci 41, 299–322. 10.1146/annurev-neuro-080317-062155. [PubMed: 29709205]

Morales M, Colicos MA, and Goda Y (2000). Actin-dependent regulation of neurotransmitter release at central synapses. Neuron 27, 539–550. 10.1016/s0896-6273(00)00064-7. [PubMed: 11055436]

Muddashetty RS, Nalavadi VC, Gross C, Yao X, Xing L, Laur O, Warren ST, and Bassell GJ (2011). Reversible inhibition of PSD-95 mRNA translation by miR-125a, FMRP phosphorylation, and mGluR signaling. Mol Cell 42, 673–688. 10.1016/j.molcel.2011.05.006. [PubMed: 21658607]

Nakahata Y, and Yasuda R (2018). Plasticity of Spine Structure: Local Signaling, Translation and Cytoskeletal Reorganization. Front Synaptic Neurosci 10, 29. 10.3389/fnsyn.2018.00029. [PubMed: 30210329]

Napoli I, Mercaldo V, Boyl PP, Eleuteri B, Zalfa F, De Rubeis S, Di Marino D, Mohr E, Massimi M, Falconi M, et al. (2008). The fragile X syndrome protein represses activity-dependent translation through CYFIP1, a new 4E-BP. Cell 134, 1042–1054. 10.1016/j.cell.2008.07.031. [PubMed: 18805096]

Narayanan U, Nalavadi V, Nakamoto M, Pallas DC, Ceman S, Bassell GJ, and Warren ST (2007). FMRP phosphorylation reveals an immediate-early signaling pathway triggered by group I mGluR and mediated by PP2A. The Journal of neuroscience : the official journal of the Society for Neuroscience 27, 14349–14357. 10.1523/JNEUROSCI.2969-07.2007. [PubMed: 18160642]

Nicoll RA, and Schmitz D (2005). Synaptic plasticity at hippocampal mossy fibre synapses. Nat Rev Neurosci 6, 863–876. 10.1038/nrn1786. [PubMed: 16261180]

Ostroff LE, Santini E, Sears R, Deane Z, Kanadia RN, LeDoux JE, Lhakhang T, Tsirigos A, Heguy A, and Klann E (2019). Axon TRAP reveals learning-associated alterations in cortical axonal mRNAs in the lateral amgydala. Elife 8. 10.7554/eLife.51607.

Rolls ET (2013). The mechanisms for pattern completion and pattern separation in the hippocampus. Front Syst Neurosci 7, 74. 10.3389/fnsys.2013.00074. [PubMed: 24198767]

Romer B, Krebs J, Overall RW, Fabel K, Babu H, Overstreet-Wadiche L, Brandt MD, Williams RW, Jessberger S, and Kempermann G (2011). Adult hippocampal neurogenesis and plasticity in the infrapyramidal bundle of the mossy fiber projection: I. Co-regulation by activity. Front Neurosci 5, 107. 10.3389/fnins.2011.00107. [PubMed: 21991243]

Routtenberg A (2010). Adult learning and remodeling of hippocampal mossy fibers: unheralded participant in circuitry for long-lasting spatial memory. Hippocampus 20, 44–45. 10.1002/hipo.20664. [PubMed: 19554645]

Roy S (2020). Finding order in slow axonal transport. Curr Opin Neurobiol 63, 87–94. 10.1016/j.conb.2020.03.015. [PubMed: 32361600]

Saha S, Mundia MM, Zhang F, Demers RW, Korobova F, Svitkina T, Perieteanu AA, Dawson JF, and Kashina A (2010). Arginylation regulates intracellular actin polymer level by modulating actin properties and binding of capping and severing proteins. Mol Biol Cell 21, 1350–1361. 10.1091/mbc.E09-09-0829. [PubMed: 20181827]

Sankaranarayanan S, Atluri PP, and Ryan TA (2003). Actin has a molecular scaffolding, not propulsive, role in presynaptic function. Nat Neurosci 6, 127–135. 10.1038/nn1002. [PubMed: 12536209]

Sanz E, Yang L, Su T, Morris DR, McKnight GS, and Amieux PS (2009). Cell-type-specific isolation of ribosome-associated mRNA from complex tissues. Proc Natl Acad Sci U S A 106, 13939–13944. 10.1073/pnas.0907143106. [PubMed: 19666516]

Scarnati MS, Kataria R, Biswas M, and Paradiso KG (2018). Active presynaptic ribosomes in the mammalian brain, and altered transmitter release after protein synthesis inhibition. Elife 7. 10.7554/eLife.36697.

Scharkowski F, Frotscher M, Lutz D, Korte M, and Michaelsen-Preusse K (2018). Altered Connectivity and Synapse Maturation of the Hippocampal Mossy Fiber Pathway in a Mouse Model of the Fragile X Syndrome. Cereb Cortex 28, 852–867. 10.1093/cercor/bhw408. [PubMed: 28077511]

Schmidt EK, Clavarino G, Ceppi M, and Pierre P (2009). SUnSET, a nonradioactive method to monitor protein synthesis. Nat Methods 6, 275–277. 10.1038/nmeth.1314. [PubMed: 19305406]

Shestakova EA, Singer RH, and Condeelis J (2001). The physiological significance of beta -actin mRNA localization in determining cell polarity and directional motility. Proc Natl Acad Sci U S A 98, 7045–7050. 10.1073/pnas.121146098. [PubMed: 11416185]

Shigeoka T, Jung H, Jung J, Turner-Bridger B, Ohk J, Lin JQ, Amieux PS, and Holt CE (2016). Dynamic Axonal Translation in Developing and Mature Visual Circuits. Cell 166, 181–192. 10.1016/j.cell.2016.05.029. [PubMed: 27321671]

Smith HL, Bourne JN, Cao G, Chirillo MA, Ostroff LE, Watson DJ, and Harris KM (2016). Mitochondrial support of persistent presynaptic vesicle mobilization with age-dependent synaptic growth after LTP. Elife 5. 10.7554/eLife.15275.

Sutton MA, and Schuman EM (2006). Dendritic protein synthesis, synaptic plasticity, and memory. Cell 127, 49–58. 10.1016/j.cell.2006.09.014. [PubMed: 17018276]

Sutula TP, and Dudek FE (2007). Unmasking recurrent excitation generated by mossy fiber sprouting in the epileptic dentate gyrus: an emergent property of a complex system. Prog Brain Res 163, 541–563. 10.1016/S0079-6123(07)63029-5. [PubMed: 17765737]

Toni N, and Schinder AF (2015). Maturation and Functional Integration of New Granule Cells into the Adult Hippocampus. Cold Spring Harb Perspect Biol 8, a018903. 10.1101/cshperspect.a018903. [PubMed: 26637288]

Treves A, Tashiro A, Witter MP, and Moser EI (2008). What is the mammalian dentate gyrus good for? Neuroscience 154, 1155–1172. 10.1016/j.neuroscience.2008.04.073. [PubMed: 18554812]

Tsang B, Arsenault J, Vernon RM, Lin H, Sonenberg N, Wang LY, Bah A, and Forman-Kay JD (2019). Phosphoregulated FMRP phase separation models activity-dependent translation through bidirectional control of mRNA granule formation. Proc Natl Acad Sci U S A 116, 4218–4227. 10.1073/pnas.1814385116. [PubMed: 30765518]

van Praag H, Kempermann G, and Gage FH (2000). Neural consequences of environmental enrichment. Nat Rev Neurosci 1, 191–198. 10.1038/35044558. [PubMed: 11257907]

Wilhelm BG, Mandad S, Truckenbrodt S, Krohnert K, Schafer C, Rammner B, Koo SJ, Classen GA, Krauss M, Haucke V, et al. (2014). Composition of isolated synaptic boutons reveals the amounts of vesicle trafficking proteins. Science 344, 1023–1028. 10.1126/science.1252884. [PubMed: 24876496]

Yang YM, Arsenault J, Bah A, Krzeminski M, Fekete A, Chao OY, Pacey LK, Wang A, Forman-Kay J, Hampson DR, and Wang LY (2018). Identification of a molecular locus for normalizing dysregulated GABA release from interneurons in the Fragile X brain. Mol Psychiatry. 10.1038/s41380-018-0240-0.

Yin HH, Davis MI, Ronesi JA, and Lovinger DM (2006). The role of protein synthesis in striatal long-term depression. J Neurosci 26, 11811–11820. 10.1523/JNEUROSCI.3196-06.2006. [PubMed: 17108154]

Yoon YJ, Wu B, Buxbaum AR, Das S, Tsai A, English BP, Grimm JB, Lavis LD, and Singer RH (2016). Glutamate-induced RNA localization and translation in neurons. Proc Natl Acad Sci U S A 113, E6877–E6886. 10.1073/pnas.1614267113. [PubMed: 27791158]

Younts TJ, Monday HR, Dudok B, Klein ME, Jordan BA, Katona I, and Castillo PE (2016). Presynaptic Protein Synthesis Is Required for Long-Term Plasticity of GABA Release. Neuron 92, 479–492. 10.1016/j.neuron.2016.09.040. [PubMed: 27764673]

Zhang Y, Brown MR, Hyland C, Chen Y, Kronengold J, Fleming MR, Kohn AB, Moroz LL, and Kaczmarek LK (2012). Regulation of neuronal excitability by interaction of fragile X mental retardation protein with slack potassium channels. J Neurosci 32, 15318–15327. 10.1523/JNEUROSCI.2162-12.2012. [PubMed: 23115170]

Zhao S, Studer D, Graber W, Nestel S, and Frotscher M (2012). Fine structure of hippocampal mossy fiber synapses following rapid high-pressure freezing. Epilepsia 53 Suppl 1, 4–8. 10.1111/j.1528-1167.2012.03469.x. [PubMed: 22612803]

Highlights

- Mossy fiber boutons (MFBs) contain ribosomes and synthesize protein locally
- Local presynaptic translation is increased by in vitro and in vivo GC activity
- MFB structural plasticity relies on de novo protein synthesis
- Presynaptic FMRP is required for MF-CA3 structural and functional plasticity

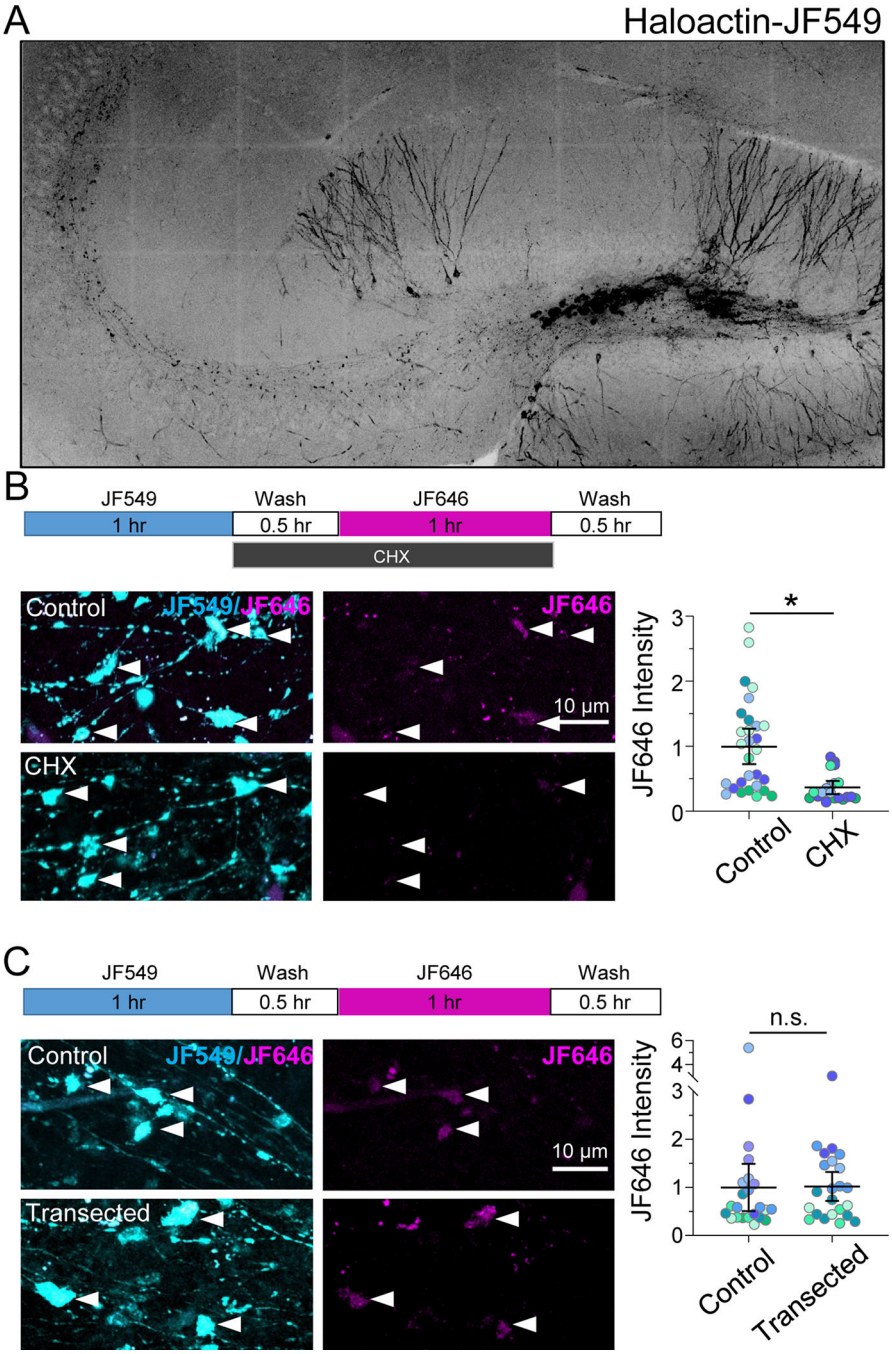

Figure 1. MFs synthesize protein locally.

A. Representative tiled fluorescence image of a hippocampal slice expressing Halo-actin labeled with JF549 HaloTag ligand after targeted stereotactic injection in dentate gyrus. B. CHX bath application blocks labeling of newly synthesized Halo-actin (JF646) in individual MF boutons. (Top) Timeline of Halo-actin pulse-chase experiment. (Bottom left) Representative images of JF549/JF646 (cyan/magenta) labeled Halo-actin in mossy fiber boutons (arrowheads) from Control or CHX-treated slices. (Bottom right) Control: 1.00 ±

0.17 vs. CHX: 0.36 ± 0.06 (Mean ± S.E.M. of slices), Mann-Whitney, U = 1, p = 0.03; n = 29, 20 boutons; 5, 4 slices respectively; 4 animals.

C. Transected mossy fiber axons synthesized β-actin protein at the same levels as intact control axons. (Top) Timeline of Halo-actin pulse-chase experiment. (Bottom left) Representative images of JF549/JF646 (cyan/magenta) labeled Halo-actin in mossy fiber boutons (arrowheads) from control or transected slices. (Bottom right) Control: 1.01 ± 0.28 vs. transected: 0.99 ± 0.26 (Mean ± S.E.M. of slices), Mann-Whitney, U = 28, p > 0.999; n = 23 boutons, 8, 7 slices respectively; 4 animals.

N = slices. Black line and bar represent the mean ± 95% confidence interval of boutons. Points representing individual boutons are color-coded by slice and normalized to mean of Control.

See also Supp. Figure 1.

n.s. = p>0.05; *p≤0.05; **p≤0.01; ***p≤0.001; ****p≤0.0001.

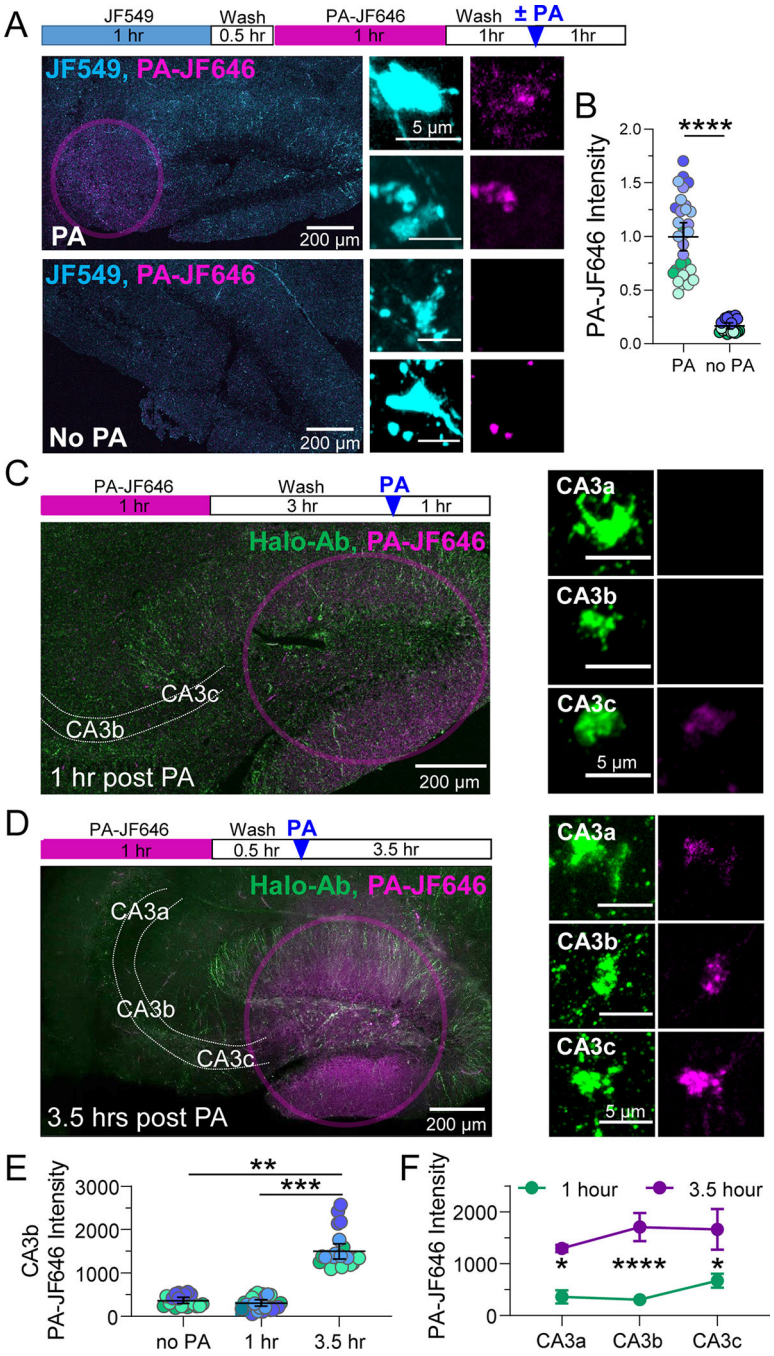

Figure 2. Locally synthesized actin contributes to MFB actin pool within 1 hour.

A. (Top) Timeline of Halo-actin pulse-chase photoactivation (PA) experiment. (Left, bottom) Representative tiled images of slices from Halo-actin injected mice incubated with JF549, followed by PA-JF646, then photoactivated in stratum lucidum (pink circle) or no PA for controls. (center) MFBs from slices that underwent PA had significantly greater levels of newly synthesized Halo-actin than those with no PA (scale bar = 5 µm).

B. Quantification of locally synthesized Halo-actin measured by intensity of PA-JF646 inside MFBs identified using JF549. PA: 2144.0 ± 137.2 v. no PA: 359.7 ± 29.2 (Mean ±

S.E.M.); Mann-Whitney, U = 0, $p < 0.0001$. n = 31, 20 boutons, 5,3 slices respectively, 3 animals.

C. (Left, top) Timeline of 1 hour post Halo-actin PA experiment. (Left, bottom) Representative tiled images of slices from Halo-actin injected mice photoactivated in DG (pink circle) 1 hour prior to fixation. (Right) Representative images of MFBs 1 hour after PA at different distances from the DG somas (CA3a, CA3b, CA3c) with Halo-actin labeled using Halo-Ab staining (scale bar = 5 μm).

D. (Left, top) Timeline of 3.5 hour post Halo-actin PA experiment. (Left, bottom) Representative tiled images of slices from Halo-actin injected mice photoactivated in DG (pink circle) at 3.5 hours prior to fixation. (right) Representative images of MFBs with all Halo-actin labeled using Halo-Ab staining at different distances from the DG somas (CA3a, CA3b, CA3c) 3.5 hours after PA (scale bar = 5 μm).

E. Quantification of PA-JF646 mean intensity in single MFBs revealed that there was no significant difference between Halo-actin levels slices with no PA vs slices that were fixed 1 hour after PA in the CA3b region where electrophysiological recordings of MF-LTP are performed. After 3.5 hours, PA-Halo-actin from DG is detectable in CA3b MFBs. No PA: 344.4 ± 78.5 v. 1 hour: 307.8 ± 55.8 v. 3.5 hours: 1582.0 ± 254.4 (Mean ± S.E.M. of slices); One-Way ANOVA with Tukey's test for Multiple Comparisons, $F [2,9] = 21.79$, $p < 0.001$. n = 20, 24, 24 boutons, 3,5,4 slices respectively, 3–4 animals. N = slices.

F. Summary data of mean intensity averaged by slice show significant increases in all CA3 subregions 3.5 hours v. 1 hour after PA. Two-Way ANOVA with Sidak's Test for Multiple Comparisons, $F[1,21] = 48.54$, $p < 0.0001$. n = 5 slices (1 hr), 4 slices (3.5 hours) 4 animals. Black line and bar represent the mean ± 95 % confidence interval of boutons. Points representing individual boutons are color-coded by slice.

n.s. = $p>0.05$; *$p\leq0.05$; **$p\leq0.01$; ***$p\leq0.001$; ****$p\leq0.0001$.

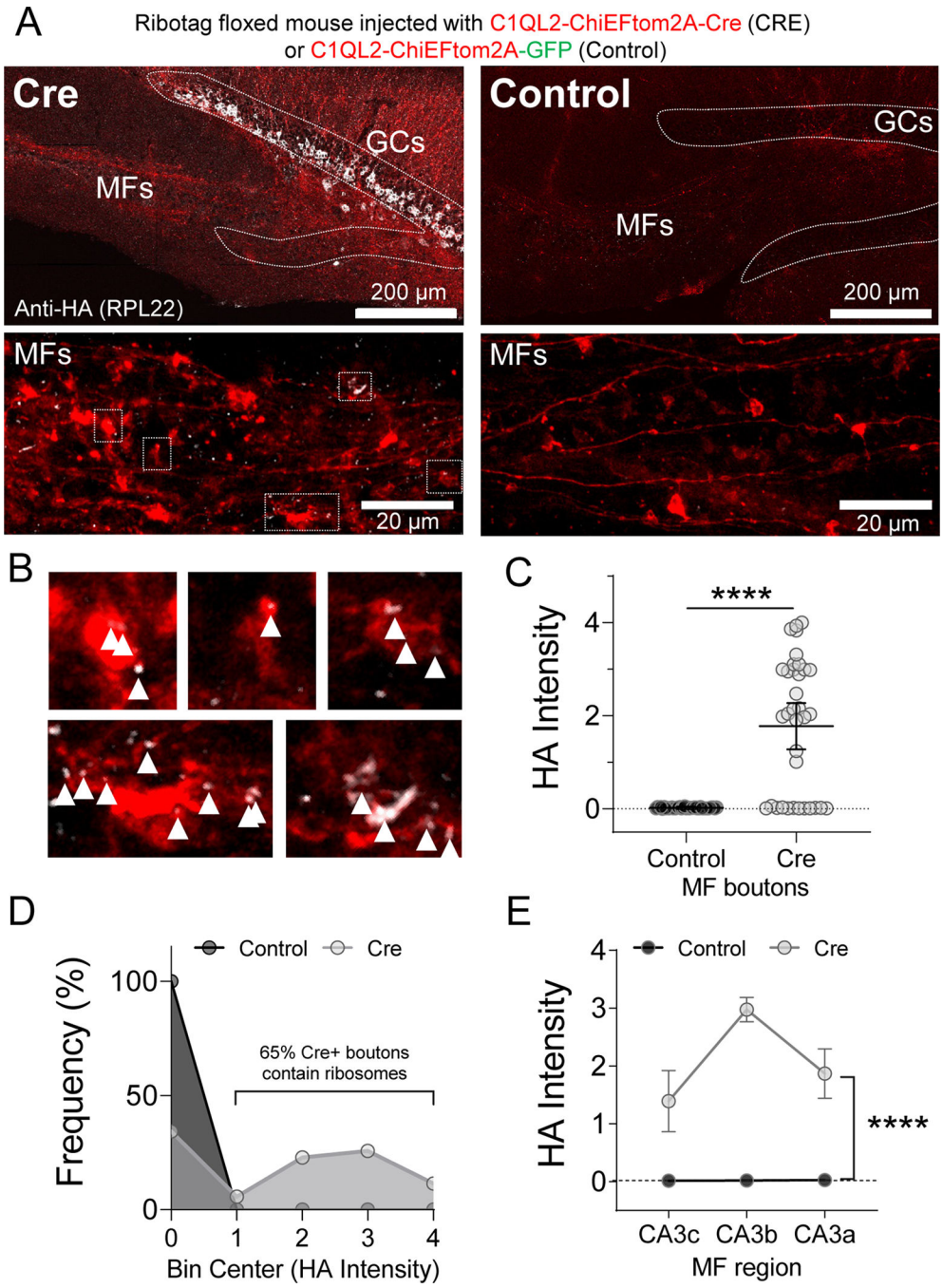

Figure 3. Ribotag mouse reveals MF axons and boutons contain ribosomes

A. (Top) Representative tiled image of hippocampal slice from Ribotag transgenic mouse injected with lentivirus encoding for ChIEF-tdTomato driven by C1QL2 promoter for dentate GC-specific expression. Dashed line indicates outline of granular layer in dentate gyrus. (Bottom) Magnification of MF boutons and axons show HA labeling in Cre+ slices. White boxes indicate magnified boutons shown in panel B.

B. Magnification of Cre+ MFBs with HA puncta indicated by white arrowheads. Clustering is noted in some boutons.

C. HA intensity inside Cre+ MFBs is significantly increased compared to GFP Controls with no HA expression. Control: 0.020 ± 0.002 v. Cre: 1.77 ± 0.25 (Mean ± S.E.M.); Mann-Whitney, U = 264.5, $p < 0.0001$. n = 39, 35 boutons, 7, 5 slices respectively, 4 animals.

D. Relative frequency (%) histogram of HA intensity values showed that ~ 65% of Cre+ MFBs contain ribosomes (MFBs with >10 fold Control levels) compared to 0% in Control slices.

E. HA intensity was significantly greater at all distances from the GC soma and highest in the CA3b region. Two-Way ANOVA with Tukey's test for Multiple Comparisons $F[1,55] = 5.82$, $p < 0.0001$, CA3b:Cre vs. CA3c:Cre, $p < 0.01$, n = 33, 28 boutons, 6, 4 slices respectively, 4 animals.

n.s. = $p>0.05$; *$p\leq0.05$; **$p\leq0.01$; ***$p\leq0.001$; ****$p\leq0.0001$.

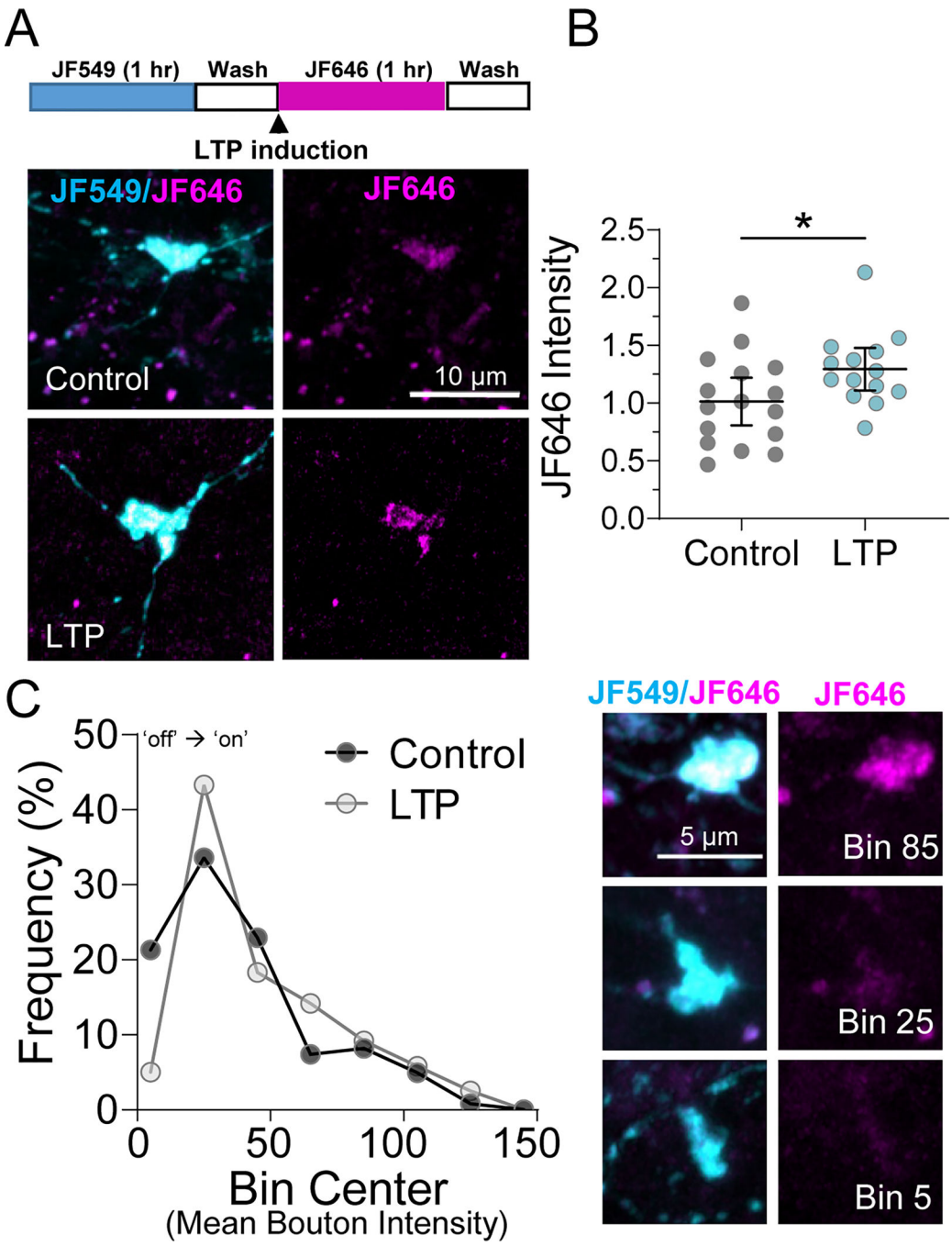

Figure 4. LTP induction elicits changes in local actin synthesis in MF tract

A. (Top) Timeline of Halo-actin LTP experiment. (Bottom) Representative images of pulse-chase labeled mossy fiber boutons in Halo-actin injected slices from CTRL v. LTP slices.

B. MF-LTP increased newly synthesized Halo-actin in individual MF boutons CTRL: 1.0 ± 0.10 v. LTP: 1.29 ± 0.09 (Mean ± S.E.M. of slices); Unpaired t-test, $p = 0.04$, $n = 122$, 120 boutons 16,14 slices respectively, 8 animals. Black line and bar represent the mean ± 95 % confidence interval of slices. Points representing average bouton intensity per slice are normalized to mean of Control.

C. (Left) Relative frequency (%) histogram of bouton intensity values indicated LTP primarily impacts low intensity boutons, shifting translationally quiescent boutons (i.e. Bin Center 5) to a translationally active state (i.e. Bin Center ≥ 25), KS test, $p = 0.04$, $n = 122$, 120 boutons 16,14 slices respectively, 8 animals. (Right) Representative boutons from indicated Bins corresponding to histogram on left.

N = slices.

n.s. = $p>0.05$; *$p\leq0.05$; **$p\leq0.01$; ***$p\leq0.001$; ****$p\leq0.0001$.

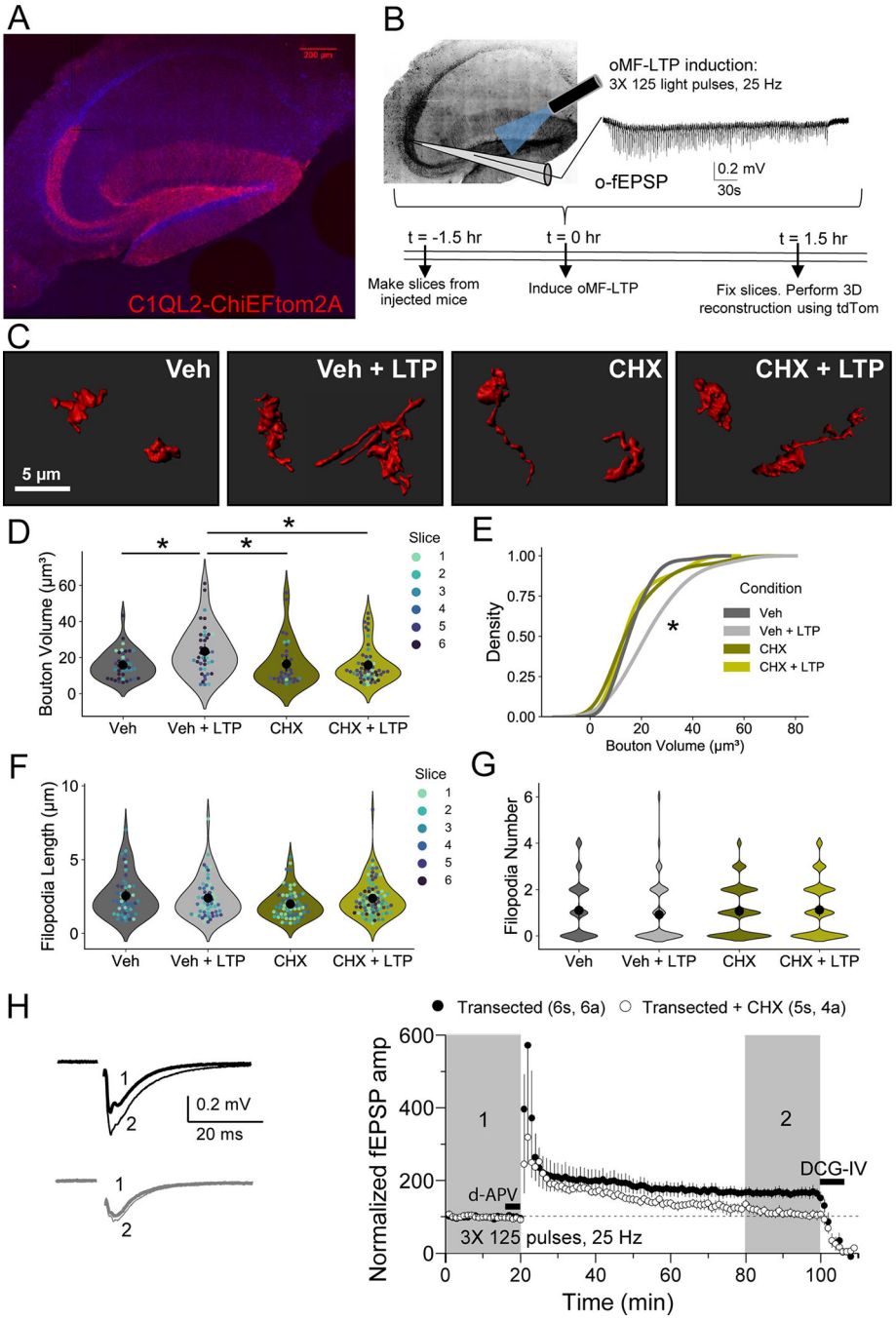

Figure 5. Structural and functional plasticity of MFBs requires protein synthesis

A. Representative tiled image of acute hippocampal slice from WT C57 mice injected with C1QL2-ChiEFtom2A-GFP.

B. Representative optogenetically-induced, extracellular field excitatory postsynaptic potentials (o-fEPSPs) recorded in CA3 resulting from optogenetic light activation (470 nm) in the hilus of slices from A. using MF-LTP induction protocol (125 pulses, 25 Hz, 3×).

C. Representative 3D reconstructions of giant MFBs from slices in A.

D. Quantification of MFB volume (μm^3) from 3D reconstructions revealed MF-LTP significantly increased bouton volume 1 hour post-LTP. This increase was blocked by bath application of protein synthesis inhibitor, cycloheximide (CHX, 80 μM). Veh: 14.24 ± 1.34 v. Veh + LTP: 24.31 ± 2.09 v. CHX: 14.84 ± 3.94 v. CHX + LTP: 13.91 ± 1.30; Two-Way ANOVA with Tukey's test for Multiple Comparisons $F[1,19] = 5.82$, $p = 0.024$, n = 41, 41, 36, 54 boutons respectively, 6 slices, 3 animals.

E. LTP induction resulted in significant shift in the distribution of bouton volume when protein synthesis is intact. KS test, $Z = 3.11$, $p < 0.00001$.

F. Length of filopodia was not altered by LTP induction or blockade of protein synthesis. Veh: 1.10 ± 0.18 v. Veh + LTP: 0.91 ± 0.16 v. CHX: 1.10 ± 0.11 v. CHX + LTP: 1.12 ± 0.14; Two-Way ANOVA with Tukey's test for Multiple Comparisons $F[1,252] = 3.00$, $p = 0.08$, n = 52, 57, 64, 83 filopodia respectively, 6 slices, 3 animals.

G. Number of filopodia per bouton was not altered by LTP induction or blockade of protein synthesis. Veh: 1.10 ± 0.18 v. Veh + LTP: 0.92 ± 0.16 v. CHX: 1.07 ± 0.12 v. CHX + LTP: 1.12 ± 0.14; Two-Way ANOVA with Tukey's test for Multiple Comparisons $F[1,263] = 0.63$, $p = 0.43$, n = 48, 62, 83, 74 boutons respectively, 6 slices, 3 animals.

H. MF-LTP was intact in transected slices, but blocked by bath application of cycloheximide (CHX, 80 μM). Transected: 164.92 ± 13.66 v. transected + CHX: 111.32 ± 11.75; Two sample t-test, $p = 0.018$, n = 5s, 4a (Transected + CHX) 6s, 6a (Transected).

N = slices. Individual points representing boutons are color-coded by slice. Large black circle and bar represent the mean ± 95 % confidence interval of boutons. See also Supp. Figure 2.

n.s. = $p>0.05$; *$p\leq0.05$; **$p\leq0.01$; ***$p\leq0.001$; ****$p\leq0.0001$.

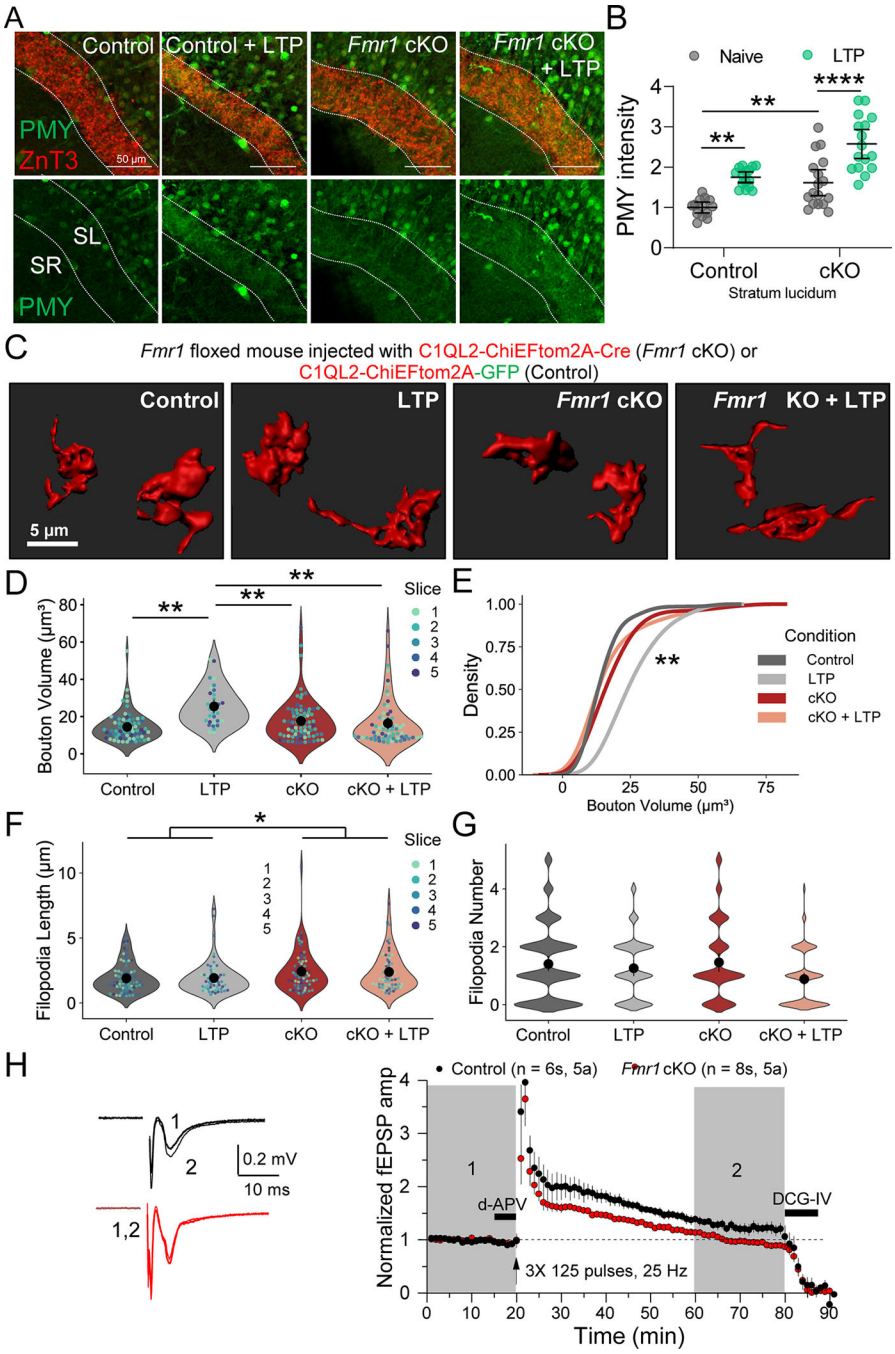

Figure 6. Presynaptic FMRP regulates MF activity-dependent protein synthesis and structural and functional plasticity

A. (*Top*) Representative images of puromycin labeling (PMY) in slices from *Fmr1*$^{fl/fl}$ mice injected with CAMKII-mCherry-Cre or CAMKII-mCherry for WT and *Fmr1* cKO. Dotted lines indicate the MF tract (stratum lucidum, SL) labeled with marker ZnT3. The stratum radiatum (SR) was measured as a control. LTP was induced with electrical stimulation (3X 125 pulses, 25 Hz).

B. *Fmr1* cKO increased PMY labeling in SL under basal conditions and with LTP induction. WT: 1.00 ± 0.03 v. WT + LTP: 1.75 ± 0.08 v *Fmr1* cKO: 1.62 ± 0.07 v. *Fmr1* cKO

+ LTP: 2.58 ± 0.06 (Mean ± S.E.M.); Two-Way ANOVA with Tukey's test for Multiple Comparisons, Genotype: F[1,57] = 30.94, p < 0.0001, Condition: F[1,57] = 43.5, p < 0.0001. n = 13, 15, 17, 16 slices respectively, 8 mice. Points represent individual slices and are normalized to mean of WT.

C. Representative 3D reconstructions of giant MF boutons from *Fmr1*$^{fl/fl}$ mice injected with lentivirus encoding C1QL2-ChiEFtom2A-Cre (*Fmr1* cKO) or C1QL2-ChiEFtom2A-GFP (CTRL).

D. MF bouton volume is increased by LTP induction in WT mice but not in FMRP cKO. CTRL: 13.64 ± 0.88 v. CTRL+ LTP: 26.43 ± 2.17 v. *Fmr1* cKO: 15.59 ± 1.73 v. *Fmr1* cKO + LTP: 15.46 ± 2.98 (Mean ± S.E.M. of slices). Two-Way ANOVA with Tukey's test for Multiple Comparisons, F[1,16] = 17.85, p = 0.0069; n = 70, 32, 76, 65 boutons respectively, 5 slices, 5 animals. In rest of superplots in this figure, individual points representing boutons are color-coded by slice. Large black circle and bar represent the mean ± 95 % confidence interval of boutons. N = slices.

E. LTP induction results in significant shift in the distribution of bouton volume. KS test, Z = 1.8, p = 0.002

F. Length of filopodia was not altered by LTP induction but is enhanced by presynaptic FMRP KO. CTRL: 1.96 ± 0.15 v. CTRL + LTP: 1.93 ± 0.24 v. *Fmr1* cKO: 2.42 ± 0.09 v. *Fmr1* cKO + LTP: 2.45 ± 0.23 (Mean ± S.E.M. of slices). Two-Way ANOVA with Tukey's test for Multiple Comparisons, Interaction: F[1,16] = 0.026, p = 0.87, Genotype: F[1,16] = 6.42, p = 0.022; n = 77, 61, 72, 62 filopodia respectively, 5 slices, 5 animals.

G. Number of filopodia per bouton was not changed. WT: 1.41 ± 0.19 v. WT-LTP: 1.26 ± 0.15 v. cKO: 1.45 ± 0.25 v. cKO-LTP: 0.85 ± 0.10 (Mean ± S.E.M. in slices). Two-Way ANOVA with Tukey's test for Multiple Comparisons Interaction: F[1,16] = 1.5, p = 0.24, n = 101, 58, 76, 75 boutons respectively, 5 slices, 5 animals.

H. (*Left*) Representative EPSPs from extracellular field recording pre- and post-MF-LTP from acute hippocampal slices of *Fmr1*$^{fl/fl}$ mice injected with AAV5-CAMKII-mCherry-Cre or AAV5-CAMKII-mCherry to KO presynaptic FMRP. (*Right*) Summary time-course plot of MF-LTP recordings show MF-LTP was blocked by presynaptic *Fmr1* KO. WT: 124.66 ± 8.47 v. cKO 99.17 ± 1.92 (Mean ± S.E.M.). Two-sample t-test, p = 0.006.

See also Supp. Figures 3 and 4.

n.s. = p>0.05; *p≤0.05; **p≤0.01; ***p≤0.001; ****p≤0.0001.

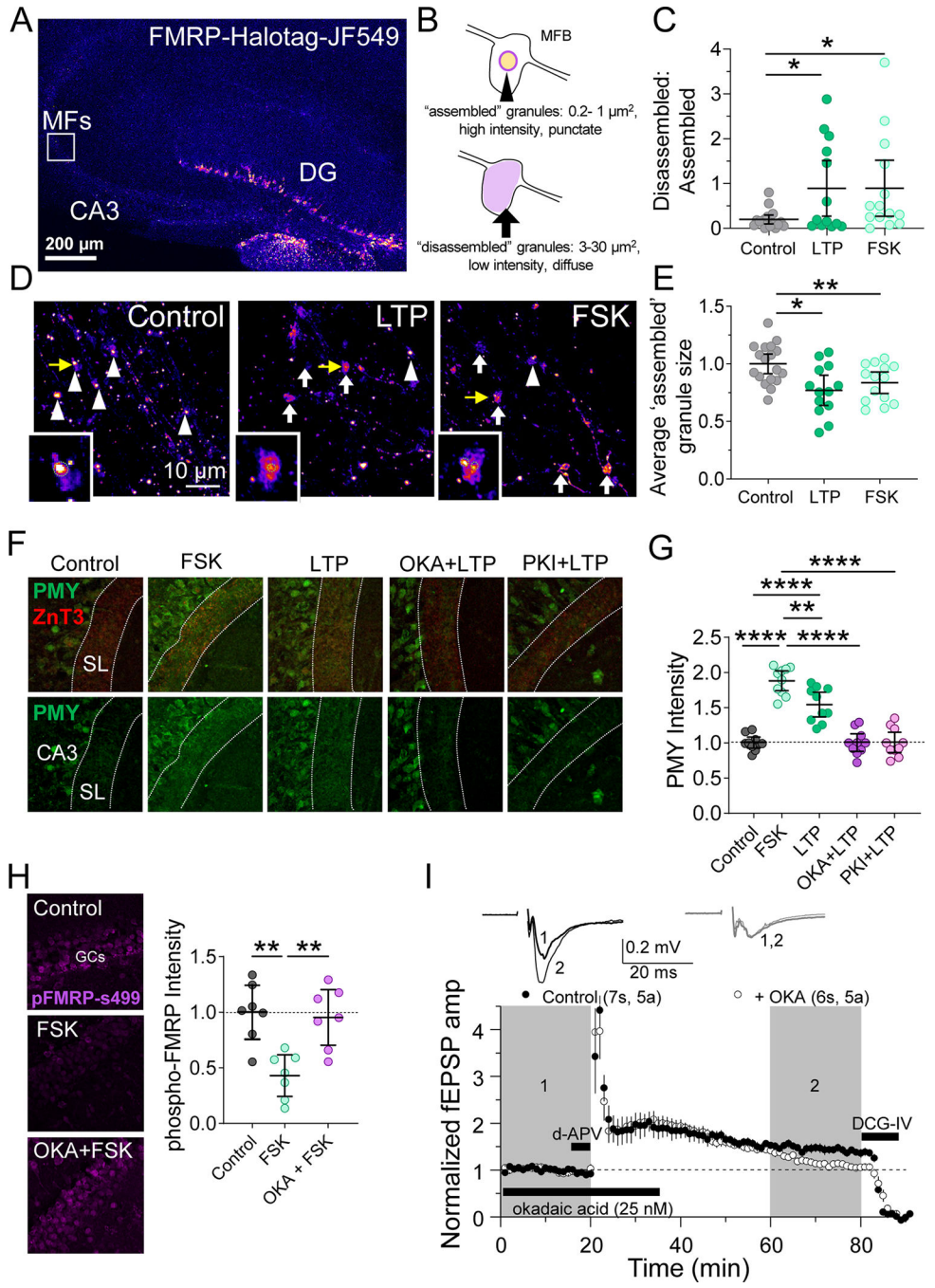

Figure 7. PKA and PP2A regulate activity-dependent FMRP granule assembly, protein synthesis, FMRP phosphorylation, and MF-LTP.

A. (*Left*) Representative tiled image of mouse hippocampal slice expressing FMRP-Halotag fusion protein in GCs.

B. Schematic of parameters defining ‘ assembled’ FMRP granules and ‘ disassembled’ granules.

C. Ratio of ‘ assembled’ to ‘ disassembled’ granules was reduced by electrical MF-LTP or chemical LTP induction with forskolin (50 µM, 10 min). CTRL: 0.197 ± 0.05 v. LTP:

0.891 ± 0.3 v. FSK: 0.894 ± 0.3 (Mean ± S.E.M.); One-Way ANOVA with Tukey's test for Multiple Comparisons, F[2,42] = 3.828, p = 0.0297; n = 18, 13, 11 slices respectively

D. Representative images of MFBs expressing Halo-FMRP. High intensity large ' assembled' granules in MFBs are indicated with white arrowheads and low intensity, diffuse ' disassembled' granules are indicated with white arrows. Insets are granules indicated with yellow arrows. Green dotted line represents contour of ' assembled' granule area quantified in panel F.

E. MF-LTP induction with electrical stimulation (3X 125 pulses, 25 Hz) or forskolin (50 μM, 10 min) reduced average size of ' assembled' granules after 10 minutes. CTRL: 1.00 ± 0.04 v. LTP: 0.77 ± 0.06 v. FSK: 0.84 ± 0.04 (Mean ± S.E.M.); One-Way ANOVA with Tukey's test for Multiple Comparisons, F[2,42] = 6.65, p = 0.003; n = 18, 13, 11 slices respectively.

F. (*Top*) Representative images of puromycin labeling (PMY) in slices from WT mice treated with PKA activator, forskolin (fSk, 50 μM) or PP2A inhibitor okadaic acid (OKA, 25 nM) or PKA inhibitor PKI (1 μM) Dotted lines indicate the MF tract (stratum lucidum, SL) labeled with marker ZnT3. LTP was induced with electrical stimulation (3X 125 pulses, 25 Hz).

G. Protein synthesis in the MF induced tract was increased by PKA activation and electrical LTP induction. This increase in protein synthesis was blocked by inhibition of PP2A and PKI. CTRL: 1.0 ± 0.03 v. FSK: 1.88 ± 0.06 v. LTP: 1.54 ± 0.08 v. OKA + LTP: 1.00 ± 0.06 v. PKI + LTP: 1.01 ± 0.06 (Mean ± S.E.M. of slices, normalized to Control); One-Way ANOVA with Tukey's test for Multiple Comparisons, F [4,45] = 45.29, p < 0.0001. n = 10 slices, 4 animals.

H. (*Left*) Representative images of hippocampal slice stained for p-FMRP-(Ser499). (*right*) Quantification of pFMRP intensity reveals phosphorylation of FMRP was decreased by PKA activation in a PP2A-dependent manner. CTRL: 1.00 ± 0.10 v. FSK: 0.43 ± 0.08 v. OKA + FSK: 0.95 ± 0.10 (Mean ± S.E.M. of slices); One-Way ANOVA with Tukey's test for Multiple Comparisons, F [2,18] = 11.47, p = 0.0006. n = 7 slices, 4 animals.

I. (*Top*) Representative EPSPs from extracellular field recording pre- and post-MF-LTP from acute hippocampal slices. (*Bottom*) Summary time-course plot indicates MF-LTP was blocked by PP2A inhibition by OKA (25 nM). Control: 1.45 ± 0.08 v. +OKA: 1.17 ± 0.05 (Mean ± S.E.M. of last 20 min); Unpaired t-test, p = 0.015, 7 slices, 5 animals; 6 slices, 5 animals respectively.

N=slices. See also Supp. Figure 5

n.s. = p>0.05; *p≤0.05; **p≤0.01; ***p≤0.001; ****p≤0.0001.

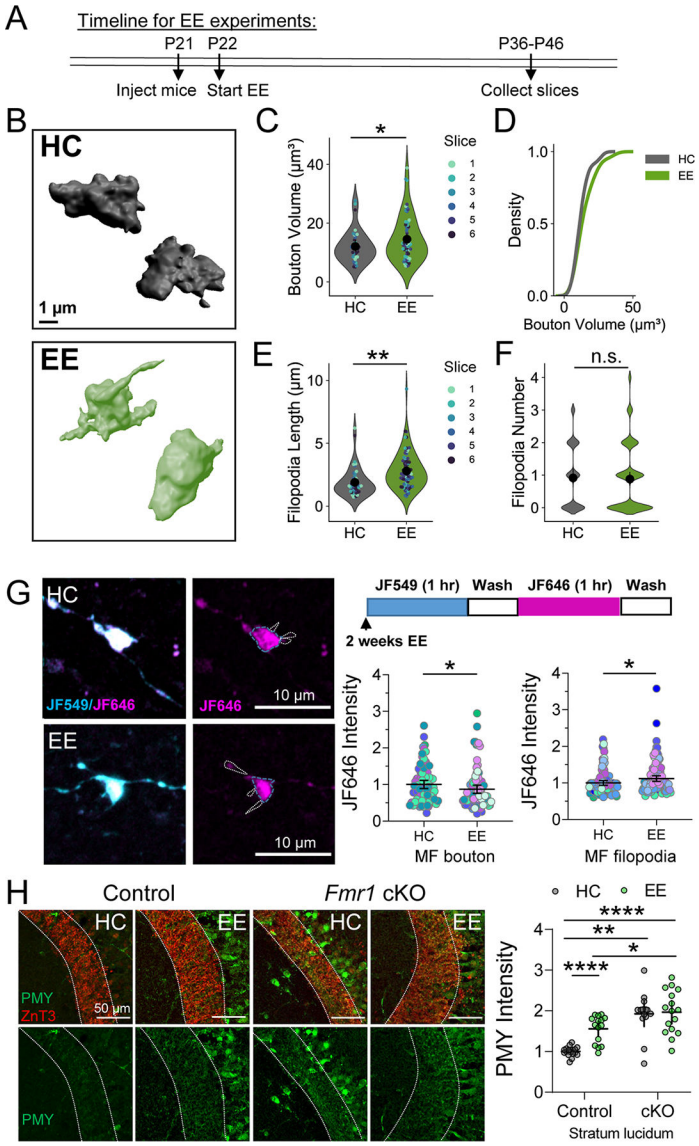

Figure 8. Enriched environment alters structural properties and local protein synthesis of MFs

A. Representative 3D reconstructions of giant MF boutons.

B. Quantification of MF bouton volume from 3D reconstructions reveals EE changed the overall volume of MF boutons. HC: 12.24 ± 0.66 v. EE: 15.16 ± 1.12 (Mean ± S.E.M. of slices); Two sample t-test, p = 0.04; n = 97, 158 boutons respectively, 6 slices, 5 animals. For all Superplots in this figure, individual points representing boutons are color-coded by slice. Large black circle and bar represent the mean ± 95 % confidence interval of boutons.

C. EE did not alter the distribution of MF bouton volume. KS test, Z = 0.67, p = 0.79

D. EE significantly changes the length of filopodia. HC: 1.75 ± 0.11 v. EE: 2.95 ± 0.29 (Mean ± S.E.M. of slices); Two sample t-test, p = 0.002; n = 42, 80 filopodia, 7, 6 slices respectively, 5 animals.

E. EE had no effect on the number of filopodia/bouton. HC: 0.85 ± 0.14 v. EE: 0.88 ± 0.08; Mann Whitney, p =0.42; n = 47, 92 filopodia, 7, 6 slices respectively, 5 animals.

F. (*Left*) Representative images of MF boutons expressing Halo-actin virus from mice in HC or 2 weeks EE. (*Right, top*) Timeline of Halo-actin pulse-chase labeling. (*Bottom, right*) Halo-actin signal measured in MF boutons was reduced in EE mice compared to HC controls. HC: 1.00 ± 0.10 v. EE: 0.77 ± 0.05 (Mean ± S.E.M. of slices); Two sample t-test, p = 0.04. (*Bottom right*) Halo-actin signal measured in filopodia of MF boutons was increased in EE mice. HC: 1.00 ± 0.05 v. EE: 1.22 ± 0.08; Mann Whitney, U = 24, p = 0.030. n = 81, 91 boutons/ 100,121 filopodia, 10,11 slices respectively, 5 animals. Points representing individual boutons are normalized to mean of Control.

G. Enriched environment did not occlude increased puromycin labeling (PMY) of newly synthesized proteins in MFs of presynaptic cKO of *Fmr1* mice. WT HC: 1.00 ± 0.03 v. *Fmr1* cKO HC: 1.90 ± 0.14 v WT EE: 1.56 ± 0.07 v. Fmr1 cKO EE: 1.96 ± 0.13 (Mean ± S.E.M.); Two-Way ANOVA with Tukey's test for Multiple Comparisons, Interaction: $F[1,59] = 6.312$, $p = 0.015$. n = 18,14, 15, 16 slices respectively. Points represent individual slices and are normalized to mean of WT HC.

N = slices. See also Supp. Figure 6.

n.s. = $p>0.05$; *$p\leq0.05$; **$p\leq0.01$; ***$p\leq0.001$; ****$p\leq0.0001$.

KEY RESOURCES TABLE

REAGENT or RESOURCE	SOURCE	IDENTIFIER
Antibodies		
Primary Antibody Anti-FMRP	Developmental Studies Hybridoma Bank, FRAXA	Cat# 7g1-1, RRID: AB_528251
Primary Antibody Anti-HA	Abcam	Cat#Ab9110, RRID: AB_307019
Primary Antibody Anti-ZnT3	Synaptic Systems	Cat#197003, RRID: AB_10894885
Primary Antibody Anti-puromycin	EMD Millipore	Mabe343; RRID: AB_2566826
Primary Antibody HaloTag antibody	Promega Corp.	G9281, RRID: AB_713650
Primary Antibody pFMRP	PhosphoSolutions	P1125, RRID: AB_2492094
Secondary Antibody Goat Anti-Rabbit Alexa Fluor™ 647	Invitrogen	Cat#A21244 (RRID: AB_2535812)
Secondary Antibody Goat Anti-Mouse Alexa Fluor™ 647	Invitrogen	Cat#A32728 (RRID: AB_2633277)
Secondary Antibody Goat Anti-Mouse Alexa Fluor™ 568	Invitrogen	Cat#A11031 (RRID: AB_144696)
Secondary Antibody Goat Anti-Rabbit Alexa Fluor™ 488	Invitrogen	Cat#A11008 (RRID: AB_143165)
Chemicals, peptides, and recombinant proteins		
NBQX	Abcam	Cat#ab120046
NBQX	Chemical Synthesis and Drug Supply Program of the National Institute of Mental Health	N/A
D-APV	Abcam	Cat#ab120003
D-APV	Chemical Synthesis and Drug Supply Program of the National Institute of Mental Health	N/A
Forskolin	Abcam	Cat#ab120058
AM251	Abcam	Cat#ab120088
DCG-IV	Tocris Bioscience	Cat#0975
MPEP	Tocris Bioscience	Cat#1212
LY367385	Tocris Bioscience	Cat#1237
YM298198	Tocris Bioscience	Cat#2448
Cycloheximide (CHX)	Tocris Bioscience	Cat#0970
Anisomycin	ALFA Aesar	CAS No. 22862-76-6
Janelia Flour 549-Halotag ligand	Janelia Research Campus, Ashburn, VA, USA	N/A
Janelia Flour 646- Halotag ligand	Janelia Research Campus, Ashburn, VA, USA	N/A
Photoactivable-Janelia Flour 646	Janelia Research Campus, Ashburn, VA, USA	N/A
Puromycin dihydrochloride	Sigma-Aldrich	Cat#P8833
Okadaic acid	Cayman Chemical	Item No. 10011490; CAS No. 78111-17-8
PKI 14–22 amide, myristoylated	Tocris Bioscience	Cat#2546
Experimental models: Organisms/strains		
Mouse: C57BL/6NCrl	Charles River	Cat# 027; RRID:IMSR_CRL:027
Mouse: *Fmr1*$^{fl/fl}$	Dr. David Nelson, FRAXA	N/A

REAGENT or RESOURCE	SOURCE	IDENTIFIER
Mouse: RiboTag	Dr. Mary Kay Lobo, University of Maryland, Baltimore County	N/A
Recombinant DNA		
HaloTag-bActinCDS-bActinUTR-MS2V5	Singer Lab, and previously in Yoon *et al.*, 2016	Addgene plasmid #102718; RRID: Addgene_102718
Mouse Halo-FMRP (p323-hySyn-Halo-mFMRP-Wpre)	This paper	Addgene plasmid #185909
AAV-CamKII-mCherry-Cre	UNC Vector Core	N/A
AAV-CamKII-mCherry	UNC Vector Core, plasmid deposited by Dr. Karl Deisseroth, Stanford University	N/A
LV-CIQL2-ChiEFtom2A-Cre	Drs. Gaël Barthet and Christopher Mulle, Université de Bordeaux	N/A
LV-CIQL2-ChiEFtom2A-GFP	Drs. Gaël Barthet and Christopher Mulle, Université de Bordeaux	N/A
Software and algorithms		
IgorPro	Wavemetrics	https://www.wavemetrics.com/
OriginPro 2015	OriginLab	http://www.originlab.com/
Graphpad Prism 8	Graphpad	https://www.graphpad.com/scientific-software/prism/
Python 3.0	Python	https://www.python.org/download/releases/3.0/
ImageJ FIJI	ImageJ	http://imagej.net/Welcome
Imaris 9.2 software	Imaris (Oxford Instruments)	https://imaris.oxinst.com/versions/9-2